Synergistic Interactions between an Upper-Level Jet Streak and Diabatic Processes that Influence the Development of a Low-Level Jet and a Secondary Coastal Cyclone

LOUIS W. UCCELLINI,* RALPH A. PETERSEN,* KEITH F. BRILL,†
PAUL J. KOCIN* AND JAMES J. TUCCILLO**

*Laboratory for Atmospheres, NASA/Goddard Space Flight Center, Greenbelt, MD 20771
†General Sciences Corporation, Laurel, MD 20707
**Development Division, National Meteorological Center, Washington, DC 20233

(Manuscript received 26 February 1986, in final form 14 March 1987)

ABSTRACT

A series of numerical simulations is presented for the February 1979 Presidents' Day cyclone in order to understand more fully the roles played by upper-level jet streaks, the oceanic planetary boundary layer (PBL), and latent heat release in the development of a low-level jet (LLJ) and secondary cyclogenesis along the East Coast of the United States. Mesoscale model simulations with and without sensible and latent heating show that the diabatic processes, along with the jet streak circulation patterns, contribute to the enhancement of the low-level winds and the initial development of the coastal cyclone. However, *none of the mechanisms acting alone* is sufficient to yield a satisfactory simulation of the LLJ and secondary cyclogenesis. Furthermore, the model-based diagnostic analyses indicate that a synergistic interaction must exist among these processes to account for the substantial increase in the magnitude of the low-level winds and the decrease in the sea level pressure that mark the secondary cyclogenesis for this case.

The following sequence is derived from the model diagnostic study: 1) Temporally increasing divergence along the axis of an upper-tropospheric jet streak located near the crest of an upper-level ridge is associated with the development of an indirect circulation that spans the entire depth of the troposphere and is displaced to the anticyclonic side of the jet. The lower branch of the indirect circulation appears to extend northwestward from the oceanic PBL up sloping isentropic surfaces toward 700 mb over the Appalachian Mountains. 2) Sensible heating and associated moisture flux within the oceanic PBL warm and moisten the lower branch of the indirect circulation, enhancing precipitation rates and latent heat release west of the coastline. 3) The combination of a shallow direct circulation associated with a developing coastal front, sloping lower-tropospheric isentropic surfaces just to the west of the coastline, and latent heat release contributes to a vertical displacement of parcels within the lower branch of the indirect circulation as they cross the coastline. 4) The vertical displacement of the parcels in a baroclinic environment (in which the pressure gradient force changes with height) results in the rapid increase in the magnitude of the ageostrophic wind and associated unbalanced flow. This imbalance contributes to parcel acceleration, resulting in the formation of a LLJ in the lower branch of the indirect circulation over a 2 to 4 h period. 5) The increasing wind speed associated with the developing LLJ is, in turn, responsible for an increase in the horizontal mass flux divergence in the entrance region of the LLJ. The increase in the mass flux divergence in the lower troposphere just above the boundary layer makes a significant contribution to the decreasing sea-level pressure that constitutes the initial development phase of the secondary cyclone along the coast.

1. Introduction

In a recent study of major snowstorms along the East Coast of the United States, Kocin and Uccellini (1985a,b) find that a significant number of the coastal snowstorms are associated with secondary cyclogenesis near the coastline as a primary system weakens west of the Appalachian Mountains. The forecast problems associated with secondary cyclogenesis (labeled a type B cyclone by Miller, 1946) are well known and include specifying the timing and location of the redevelopment of the surface low along the coast. Kocin and Uccellini also show that the coastal cyclogenesis is often marked by an enhancement of the 850 mb wind field, which usually takes the form of a low-level jet (LLJ). The LLJ develops either as secondary cyclogenesis commences or as a coastal front/inverted trough forms prior to cyclogenesis. Maximum wind speeds can exceed 30 m s^{-1} in the core of the LLJ and are typically directed from the south, southeast, or east toward the area of heavy precipitation associated with the cyclone. The LLJ acts to increase the moisture transport toward the region of heavy precipitation. The strong warm air advection associated with large wind speeds and thermal gradients along the coast may also be an important factor in the occurrence of secondary cyclogenesis.

In the analyses of the Presidents' Day cyclone of 18 and 19 February 1979, Uccellini et al. (1984) describe the development of an intense and highly ageostrophic LLJ on 18 February, during the period in which a coastal front and inverted trough formed along the Southeast Coast. The decreasing sea-level pressure as-

sociated with the inverted trough represents the initial phase of secondary coastal cyclogenesis. The simultaneous development of a LLJ and the initial phase of secondary cyclogenesis suggests that these features may be linked.

The purpose of this paper is to describe numerical model simulations of the Presidents' Day cyclone that demonstrate the importance of dynamic and thermodynamic processes in the initial development phase of secondary cyclogenesis on 18 February 1979. The numerical simulations are used to investigate how an upper-level jet streak, an ocean-influenced planetary boundary layer, and latent heat release interact in a synergistic manner to contribute to the rapid development of the LLJ and cyclone in this case. Furthermore, diagnostic computations from the model simulations are presented to highlight the importance of the mass flux divergence associated with the LLJ in focusing the area of surface pressure falls that marks the commencement of secondary cyclogenesis along the coast.

The development of the LLJ associated with the Presidents' Day cyclone is described in section 2. The mesoscale numerical model, initial analyses, and experimental design used in this study are discussed in section 3. In section 4, four numerical simulations are discussed and compared. This experiment includes an adiabatic simulation that isolates the development of upper-level divergence along the axis of a subtropical jet streak and three other simulations that reveal the contributions of sensible and latent heat release in modifying lower-tropospheric wind fields and reducing the sea-level pressure. In section 5, the formation of the LLJ is described through an evaluation of trajectories derived from the various model simulations. The effect of the LLJ on secondary cyclogenesis along the East Coast is then described in section 6. The results are summarized in section 7.

2. Review of the Presidents' Day cyclone and description of the low-level jet during the precyclogenetic period

The Presidents' Day cyclone developed along the East Coast of the United States on 18–19 February 1979, producing heavy snow accumulations from North Carolina to southeastern New York. A variety of processes appear to have contributed to various stages of the storm's development, as described in numerous papers listed in Table 1.

Since Bosart (1981) and Uccellini et al. (1984) present detailed synoptic overviews of the storm, only a brief description is presented here. At 06Z/18,[1] snow, sleet, and rain were occurring in the southern United States with an inverted trough beginning to extend northward from the Gulf of Mexico (Fig. 1a). By 12Z/18, heavy snow developed in the southeastern United States as a separate inverted trough/coastal front began to develop off the Southeast Coast (Fig. 1b). A surface low formed along the coastal front by 18Z/18 (Fig. 1c) and moved northeastward to a position off the South Carolina coast by 00Z/19 (Fig. 1d). The development of the coastal low occurred as the primary surface low remained in the Ohio Valley (Fig. 1d). The coastal system continued to intensify, deepening explosively off the Virginia coast after 06Z/19.

The period prior to 18Z/18 was marked by significant changes in the upper- and lower-tropospheric wind fields. A subtropical jet (STJ) near 200 mb amplified on 17 and 18 February, with wind speeds increasing 5 m s^{-1} along a significant portion of the jet axis between 00Z/18 and 12Z/18 (Figs. 2a and 2b). Uccellini et al. (1984) diagnose a temporally increasing divergence field along the axis of the STJ upstream of the upper-level ridge crest during this period and suggest that the increasing divergence aloft contributed to the heavy snow in Tennessee and North Carolina (Fig. 1b). As the divergence along the axis of the STJ increased, a low-level jet (LLJ) developed in the southeastern United States. Winds near the 850 mb level on the 292 K isentropic surface increased from 5 to 25 m s^{-1} between 00Z/18 and 12Z/18 (Figs. 2c and 2d). The LLJ was directed up sloped isentropic surfaces from about 900 mb (over the ocean) toward the 700 mb level (over the Carolinas) and was an important factor in doubling the magnitude of the moisture transport into the region of heavy snow. The southeasterly LLJ formed at an angle nearly perpendicular to the coastline in a region where the geostrophic wind was south-southwest [as can be inferred from the analysis of the Montgomery streamfunction (ψ_m) in Fig. 3] and relatively weak. As a result, the rapid development of the LLJ was marked by a well-defined 20 m s^{-1} ageostrophic wind component at 12Z/18 (Fig. 3b), in an area where only an ill-defined 5 m s^{-1} ageostrophic wind field had existed 12 h earlier (Fig. 3a).

Uccellini et al. (1984) also note that the development of the LLJ occurred in the lower branch of an indirect circulation associated with the STJ. This circulation is depicted in the cross section in Fig. 4 that extends along a line from northern Illinois to a position off the Southeast Coast (Fig. 2b). The cross section was drawn along this line since it is nearly parallel to the axis of the LLJ and at a significant angle to the axis of the STJ. The horizontal branches of the circulation represent the tangential component of the ageostrophic

[1] The time and date format used in this paper is similar to that used in previous Presidents' Day storm papers (e.g., 0000 UTC 18 February is expressed as 00Z/18). All analyses in this paper were derived using Petersen's (1986) objective analysis scheme on a 2° latitude by 2° longitude grid using datasets described by Uccellini et al. (1984).

TABLE 1. Diagnostic studies of the President's Day cyclone of 18–19 February 1979.

Development phase	Phenomenon/process	Reference
Precyclogenetic period and initial secondary development (18 February)	1. Coastal frontogenesis	Bosart (1981)
	2. Diabatic processes	Bosart (1981), Bosart and Lin (1984), Uccellini et al. (1983)
	3. Increasingly divergent subtropical jet	Uccellini et al. (1983, 1984)
	4. Ageostrophic low-level jet	Uccellini et al. (1983, 1984)
Rapid development phase (19 February)	1. Large-scale forcing	Bosart (1981), Bosart and Lin (1984), Uccellini et al. (1984), Atlas (1987)
	2. Upstream tropopause folding	Uccellini et al. (1985), Petersen et al. (1985)
	3. Heating on the convective scale	Bosart (1981)
	4. Other diabatic processes	Bosart and Lin (1984), Atlas (1987), Uccellini et al. (1985)

wind interpolated to the plane of the cross section from the three-dimensional array of data, derived using the Petersen (1986) objective analysis scheme [see Fig. 10c in Uccellini et al. (1984) for the orientation of the ageostrophic streamlines associated with the STJ]. The vertical components were derived by vertically integrating the continuity equation in pressure coordinates, imposing the adjustment described by O'Brien (1970) in which the error variances for divergence are assumed to increase linearly with decreasing pressure.

The cross section depicts an indirect circulation (marked by an I in Fig. 4) that was displaced to the anticyclonic side of the STJ and is defined by the 3 μb s^{-1} descent of relatively warm air off the coast and 8 μb s^{-1} ascent of relatively colder air beneath the axis of the STJ. The upper- (lower-) tropospheric ageostrophic flow directed toward the anticyclonic (cyclonic) side of the STJ completes the circulation pattern. The displacement of the indirect circulation to the anticyclonic side of the STJ could be due to either weak inertial stability (Bjerknes, 1951; Keyser and Pecnick, 1985), the effect of warm-air advection along the flow (Keyser and Shapiro, 1986), or both. Finally, a significant portion of the troposphere beneath and on the cyclonic side of the STJ axis is marked by a large ageostrophic component directed to the left of the flow. This is consistent with the diagnosed acceleration of parcels along the axis of the STJ and near the ridge crest as discussed by Uccellini et al. (1984).

Although the indirect circulation on the anticyclonic side of the STJ is depicted on a two-dimensional plane, the vertical branches are likely affected by three-dimensional (along- and cross-stream) ageostrophic, divergent flow as noted by Uccellini et al. (1984). Nevertheless, the slope of the LLJ from beneath 850 mb to above the 700 mb level within the lower branch of the indirect circulation suggests that a coupling may exist between the upper- and lower-level jets as discussed by Uccellini and Johnson (1979). However, the occurrence of heavy precipitation beneath the axis of the STJ and the large magnitude of the sensible heating off the coast for this case (Bosart, 1981; Chou and Atlas, 1982) suggest that diabatic processes could also be influencing the observed ageostrophic wind fields, as recently discussed by Keyser and Johnson (1984) for a case involving deep convective storms. Furthermore, the location of the LLJ just above the developing coastal front (compare Figs. 1b and 2d) indicates that processes associated with coastal frontogenesis could also play a role in the formation of the LLJ. Given that a large number of physical processes may be influencing the rapid evolution of the LLJ between 00Z/18 and 12Z/18 and the subsequent development of a coastal cyclone, a series of numerical simulations is needed to assess the contributions of the adiabatic and diabatic processes in the development of the LLJ and associated sea-level pressure falls along the coast.

3. The numerical model and experimental design

a. Model description

The numerical model used in this study is an updated version of the Mesoscale Analysis and Simulation System (MASS) described by Kaplan et al. (1982a), evaluated by Koch (1985) and Koch et al. (1985), and transferred to the CYBER 205 at the Goddard Space Flight Center (Tuccillo, 1984). The vertical coordinate, σ, is defined as $(p - p_t)/(p_s - p_t)$ for 24 equally spaced levels, where p is pressure and p_s and p_t are the pressure at the surface and top (100 mb) of the model, respectively. The simulations discussed here were done on a 60 km grid for a 128 by 96 mesh corresponding to a 40 by 30 subset of the National Meteorological Center's (NMC's) Limited Area Fine Mesh (LFM) grid area covering all of North America and the western Atlantic Ocean to approximately 55° longitude.

The Koch et al. (1985) evaluation indicates that an earlier version of MASS had a systematic mass-loss problem under certain synoptic regimes along the eastern boundary. Several changes to the model eliminated this problem, including correcting the horizontal spatial derivative of the map-scale factor in the mass continuity equation and improving the boundary layer parameterization by treating separately the cases of free convection over land and water (see the Appendix). Other modifications include the following: 1) The sixth-order

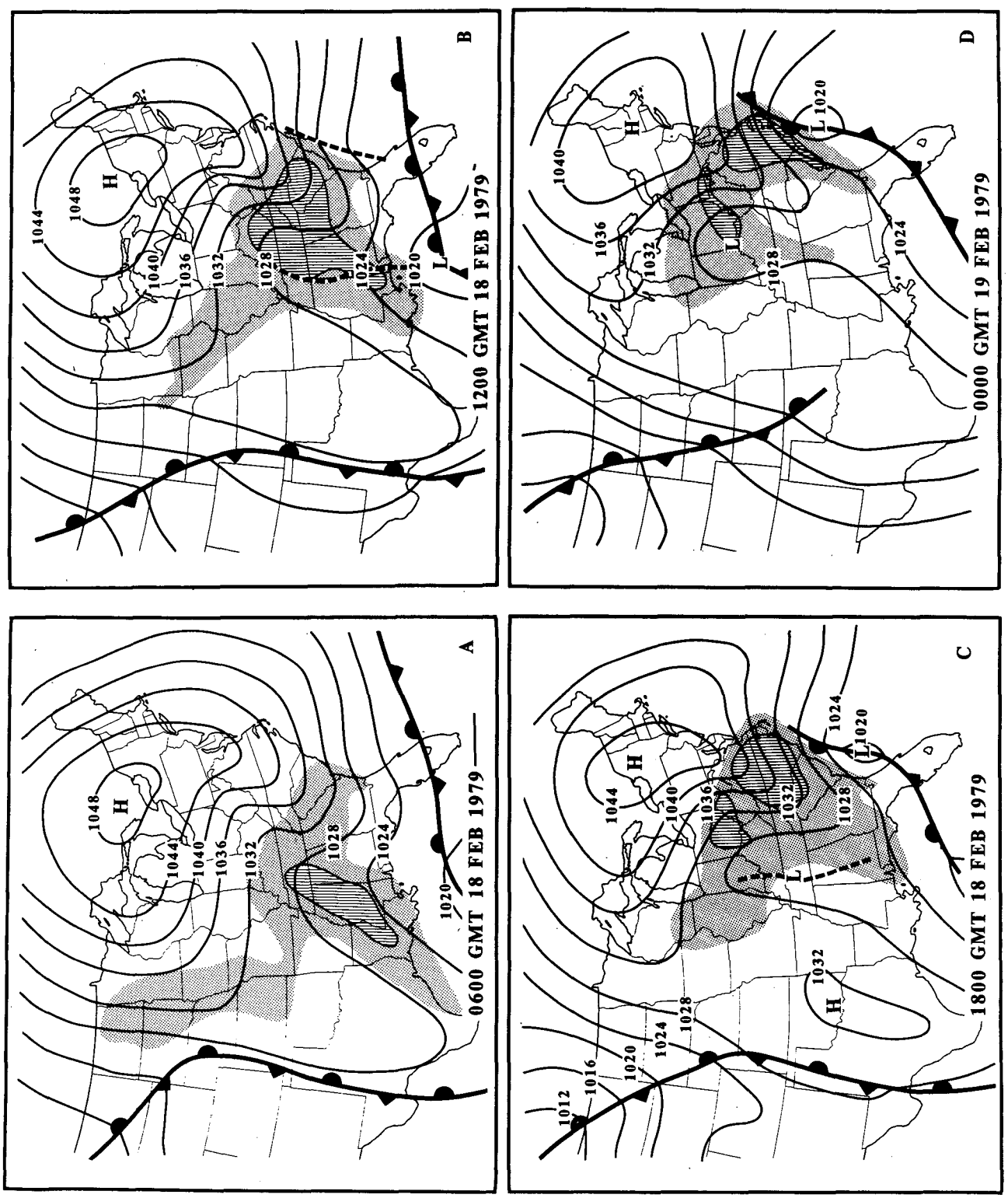

FIG. 1. Surface analyses (solid lines are isobars, mb) for (a) 0600 UTC, (b) 1200 UTC, (c) 1800 UTC 18 February, and (d) 0000 UTC 19 February 1979. Shading represents precipitation, with hatched shading representing moderate to heavy precipitation. Dashed lines in (b) and (c) indicate sea-level inverted pressure trough and developing coastal front.

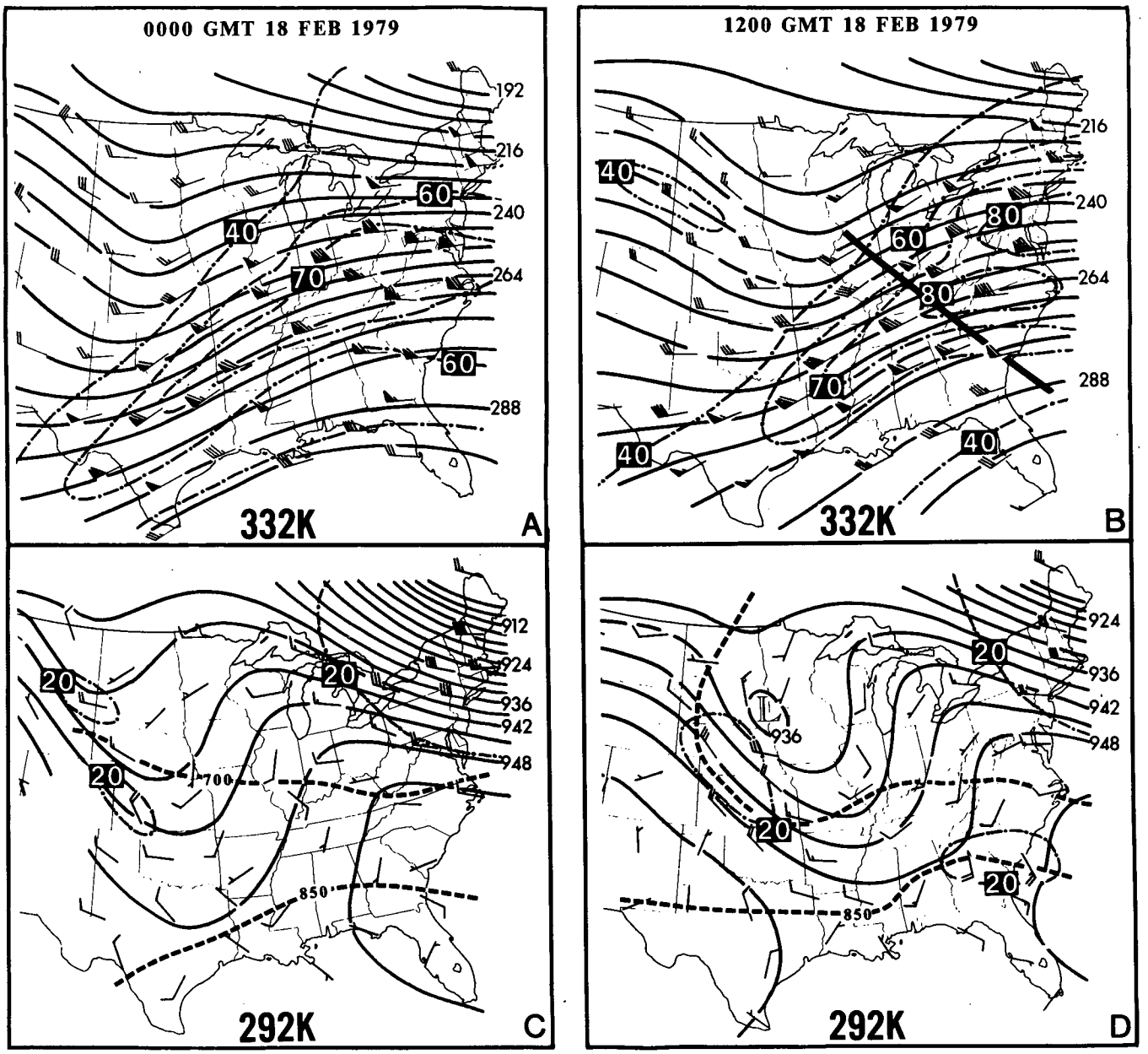

FIG. 2. Isentropic analyses for 332 K (a and b) and 292 K (c and d) at 0000 and 1200 UTC 18 February 1979, respectively. Montgomery streamfunction (ψ_m) (solid, 288 = 3.288×10^5 m^2 s^{-2}; 936 = 2.936×10^5 m^2 s^{-2}) and isotachs (dot-dashed, m s^{-1}). Wind barbs represent measured velocities (flag = 50 m s^{-1}; barb = 10 m s^{-1}; half-barb = 5 m s^{-1}). Isobars on 292 K surface are dashed (mb). Heavy line in (b) indicates position of cross section in Fig. 4.

finite differencing was replaced with fourth-order differencing. 2) The finite differencing for the mass continuity equation was changed to second order to balance the mass flux across adjacent grid volumes. 3) Data from the FGGE analysis (provided by the European Centre for Medium Range Weather Forecasts) were made an option for specifying time-dependent lateral boundary conditions. Differences between the analyses were divided by the number of time steps during the 6 h period to compute tendencies, which were then applied along the boundary at each time step.

Condensation and evaporation of grid-resolvable precipitation are included in the model. Convective precipitation is determined using a modified Kuo (1974) cumulus parameterization scheme with closure parameters specified by Molinari (1982). Diffusion is applied to the prognostic equations for the horizontal wind components, moisture, surface pressure, and

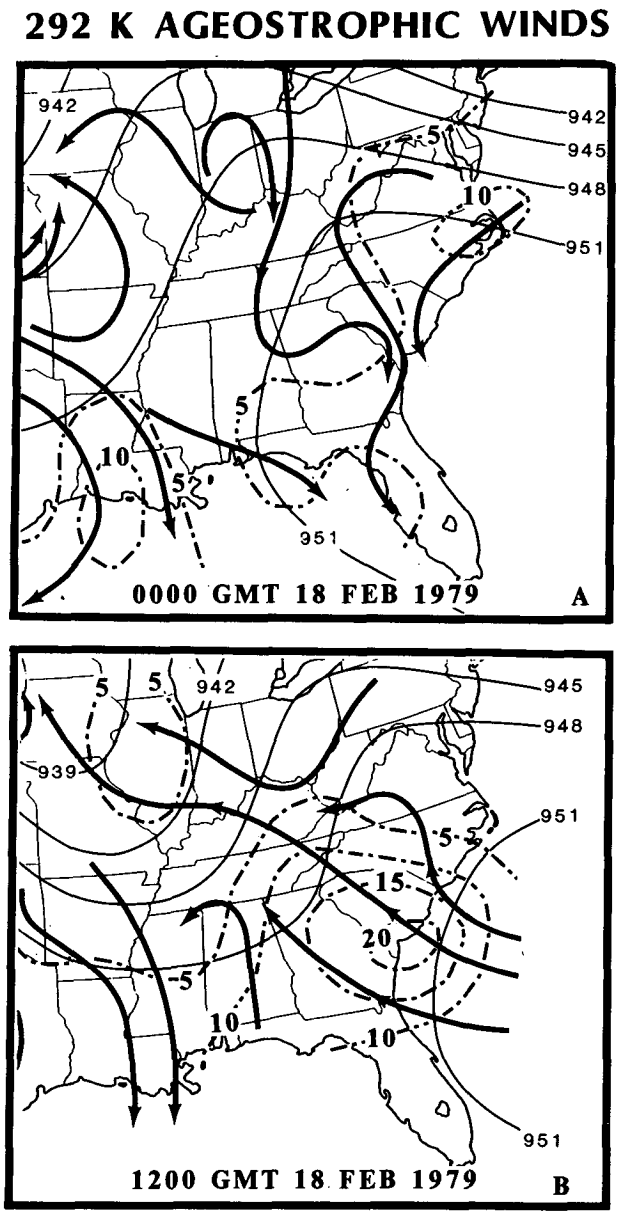

FIG. 3. Streamline (solid arrows) and isotach (dot-dashed, m s^{-1}) analyses for the ageostrophic wind field on the 292 K surface for (a) 0000 and (b) 1200 UTC 18 February 1979. Convention for ψ_m is the same (light solid lines) as used in Figs. 2c and 2d.

temperature using a $K\nabla^4$ operator where K is defined as a diffusion coefficient and is set to 5×10^5 m^4 s^{-1} on the interior grid points of the model domain. The topography used in the model is equivalent to that used in the LFM and is shown in Fig. 5c.

b. Initial analyses

For this study, the model simulations were started at 00Z/18, with temperature, moisture, and wind fields generated at 25 mb intervals using a Cressman (1959) analysis and the FGGE gridded data as a first guess. These fields were updated with an isentropic analysis of the operational radiosonde data over a major portion of the contiguous United States and 14 supplemental soundings over the ocean near the East Coast.[2] The procedure for inserting the isentropic-based analyzed fields into the model domain is described by Petersen et al. (1985). The model initialization was completed by applying a variational adjustment of temperature under hydrostatic constraint and a variational minimization of the vertically integrated mass divergence and associated surface pressure tendency.

The initial sea-level pressure (SLP) analysis at 00Z/18 (Fig. 5c) is nearly equivalent to that shown in previous studies of the Presidents' Day cyclone (see, e.g., Fig. 1b in Uccellini, 1984), with a distinct anticyclonic ridge extending southward to the east of the Appalachian Mountains. Extremely cold air associated with this surface high-pressure system is reflected in the temperature analysis on the first model σ level above the ground, which is near the 1000 mb level (Fig. 5c). The -5°C isotherm extends well to the south and east along the coast and out over the Atlantic Ocean, where the climatological sea surface temperatures (SSTs) are as high as 10° to 15°C (Fig. 5d).[3] In an extensive region off the middle Atlantic coast, the air temperature on the lowest model surface is 18° to 20°C colder than the underlying SST (Fig. 5d). The existence of the very cold air overlying the warm SST is confirmed by Figs. 11 and 12 in Chou and Atlas (1982), where the air temperature at a buoy located at 39°N, 70°W of -7°C at 15Z/17 February is 17°C colder than the 10°C SST observed at the same location (buoy location is shown in Fig. 5c). Even though the temperature difference between the lowest model sigma surface and the ocean surface is representative of the general conditions documented for this case where very cold air overlies warmer water, there is no way of verifying the accuracy of the distribution of the temperature difference (Fig. 5d) and especially of the gradients. Since 1) the analysis and initialization routines are conducted on grids ranging from 190 to 60 km and 2) the colder radiosonde reports along the coast will have significant influence on the analysis well out over the ocean, it is likely that the 12° to 18°C magnitude in the difference fields could have a different distribution than that shown in Fig. 5d, especially along the coastline. It will take a com-

[2] The supplemental soundings were generated by combining ship and buoy reports of surface pressure, temperature, winds, and dewpoint (when available) with mandatory level data derived from the LFM analyses for the locations indicated in Fig. 5c. These uniformly spaced soundings were used in an attempt to better define the initial conditions over the ocean, especially in the lowest portion of the troposphere. We recognize, however, that mesoscale detail in the temperature, wind, and moisture fields over the ocean cannot be represented in the initial conditions using this approach.

[3] The climatological SST pattern was very similar to the observed pattern for the period 14–21 February 1979 (see Fig. 12 in Chou and Atlas, 1982) and was thus used in this model study.

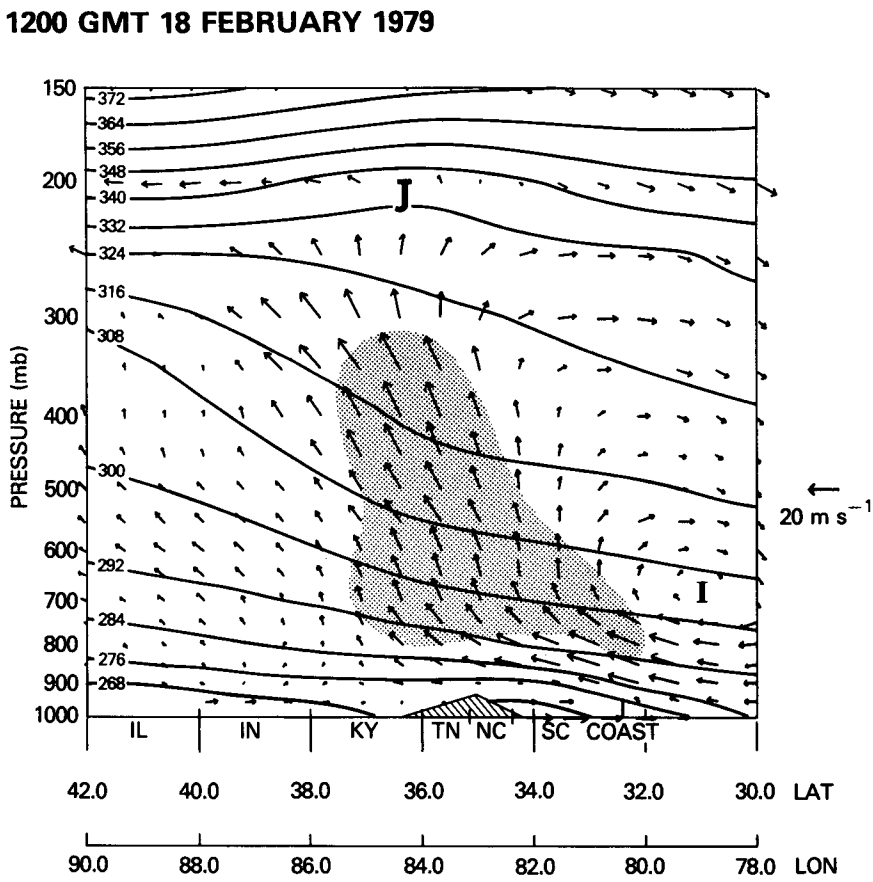

FIG. 4. Vertical cross section of potential temperature (contour interval 8 K, solid) at 1200 UTC 18 February 1979 and vector representation of ageostrophic indirect (I) circulation derived from the objective analysis scheme (see text for details). Cross section derived along rhumb line illustrated in Fig. 2b. Shading indicates region where ascent is greater than -6 μb s^{-1}. Scale for magnitudes (m s^{-1}) of horizontal component shown on right. J indicates position of core of subtropical jet streak. No inferences should be made from this figure concerning the extent of cross-isentropic flow within the two-dimensional plane of the cross section, given that only the horizontal ageostrophic wind (and not the total wind) is used in this representation of the circulation.

bination of higher-resolution models and more spatially uniform, mesoscale datasets that cover a large area over the land and ocean to fully assess the importance of this issue.

Aloft, the initialized 332 and 292 K fields shown in Figs. 5a and 5b, respectively, are nearly identical to those shown in Fig. 2. The axis of the STJ, defined by the 70 m s^{-1} contour in Fig. 5a, extends from Arkansas to Virginia. The confluence of this air stream with a west-northwesterly flow over New England contributes to the 75 m s^{-1} maximum centered over eastern Virginia. The incorporation of the variational adjustment scheme eliminates the "noise" around the perimeter of the domain in which the isentropic analysis was inserted while maintaining the 5.0×10^{-5} s^{-1} divergence maximum at the 200 mb level over Illinois (Fig. 5a), as was diagnosed for this case (see Fig. 14b in Uccellini et al., 1984).

c. *Model experiment*

This model experiment consists of four simulations, briefly summarized in Table 2. Statistical measures of accuracy were obtained for each simulation listed in Table 2 by computing the root-mean-square, bias, and S1 (Teweles and Wobus, 1954) scores for sea-level pressure (SLP) and the bias for the temperature (T) and dewpoint (Td) for the first model level above the ground (or approximately 1000 mb). The statistics are computed for a domain encompassing the region from the Mississippi River to 70°W, between 30° and 50°N.

In the adiabatic simulation (ADB), the latent heat associated with resolvable grid-scale precipitation is not incorporated into the model and the parameterizations for the boundary layer and convective subgrid-scale precipitation are not operating. Surface stress, however, is applied to the lowest model layer using a procedure

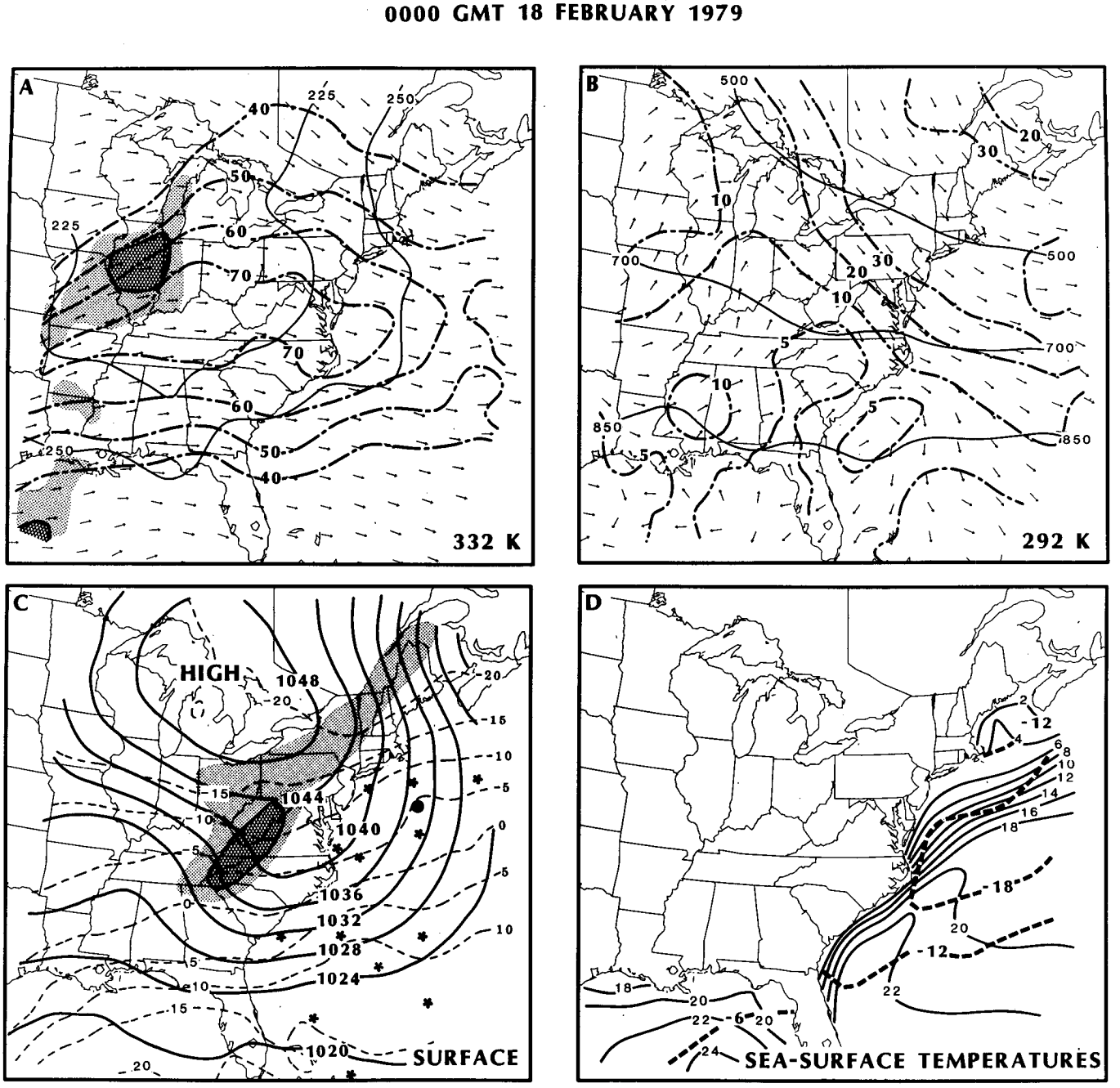

FIG. 5. Selected initial fields from 0000 UTC 18 February used in model simulations described in text: (a) isotach (m s^{-1}, dot-dashed), wind directions (arrows), and 225 and 250 mb isobars (solid) for 332 K surface. (b) As in (a), but for 292 K surface with 850, 700, and 500 mb isobars (solid). (c) Sea-level pressure (mb, solid) with topography shaded [light shading greater than 250 m above sea level (ASL); dark shading greater than 500 m ASL] and air temperature for lowest σ model level or approximately 1000 mb (°C, dashed); the locations of the supplemental soundings are indicated by an asterisk and the buoy at 39°N and 70°W by black circle. (d) Climatological sea surface temperature (°C, solid) and temperature difference between sea surface and lowest model sigma surface (°C, heavy dashed).

described by Haltiner and Williams (1980, pp. 272–274). Given the results of the recent model simulations for this case (Atlas, 1987) and other coastal storms (e.g., Anthes et al., 1983), the absence of sensible and latent heat fluxes over the Atlantic Ocean in this experiment is anticipated to result in a weaker storm system. This

TABLE 2. Summary of four model simulations of the Presidents' Day storm of 1979. Statistics computed for 12Z/18 (12 h forecast) and 00Z/19 (24 h forecast) include the root mean square error (rms), bias (in mb), and S1 score for sea-level pressure (SLP) [along with minimum SLP (mb) along Carolina coast], bias for the first model level (or near 1000 mb) temperature (T) and dewpoint (T_d) in °C, for an area encompassing approximately the eastern half of the United States.

				Statistical scores							
				SLP				1000 mb T bias		1000 mb Td bias	
				Minimum rms/bias		Minimum rms/bias					
Experiment	Boundary layer	Grid-scale precipitation	Convective precipitation	12Z/18	S1 12Z/18	00Z/19	S1 00Z/19	12Z/18	00Z/19	12Z/18	00Z/19
ADB	Off	Off	Off	1032	2.8/−0.6 40.3	1036	8.2/6.8 53.3	−2.3	−7.4	−7.8	−12.6
BLYR NO LHT	On	Off	Off	1027	3.4/−2.1 41.7	1024	3.4/2.4 46.3	2.6	−0.6	3.6	1.9
LHT NO BLYR	Off	On	On	1032	2.8/−1.1 40.9	1036	7.8/6.3 54.0	−2.6	−7.8	−6.3	−11.4
FULL PHYS	On	On	On	1024	3.8/−2.8 42.8	1017	3.0/0.1 47.5	2.5	−0.7	3.5	1.3

expectation is confirmed by the minimum SLP and the S1 scores, rms errors, and bias for the SLP listed in Table 2, which increase significantly during the last 12 h of the simulation. The increasing negative bias for the T and Td on the lowest model level between 12Z/18 and 00Z/19 also indicates that the lack of physical processes in the model results in a simulation that becomes increasingly too cold and dry.

In the second simulation (BLYR NO LHT), the boundary layer parameterization is functioning, but the latent heating associated with both the resolvable grid-scale precipitation and convective parameterization is not included. This simulation is designed to isolate the effects of heat and moisture fluxes within the oceanic planetary boundary layer (PBL) without the presence of latent heat release. The 1024 mb minimum in the SLP at 00Z/19 and statistical scores listed in Table 2 indicate a noticeable improvement in this simulation over ADB, especially with respect to removing the large biases in the 1000 mb T and Td at 00Z/19. Nevertheless, a 2.4 mb bias in the sea-level pressure is still evident at 00Z/19, which is a reflection of a weaker simulated cyclone along the coast than that observed.

In the LHT NO BLYR simulation, both the convective and resolvable grid-scale precipitation routines are operating, but the boundary layer parameterization is not included. This simulation isolates the effect of latent heat release on the coastal system without any additional heat and water vapor supplied from the ocean surface during the course of the numerical forecast. In this simulation, the minimum SLP and the statistical scores listed in Table 2 reflect little or no improvement over ADB, indicating that the separate inclusion of latent heat release did not improve the simulation of the coastal cyclone for this case.

In the FULL PHYS simulation, where all physical parameterizations are included, the rms, S1, and bias scores are significantly better than those in ADB and LHT NO BLYR and equivalent to BLYR NO LHT (Table 2). While the magnitudes of the rms errors and S1 scores in the FULL PHYS simulation are nearly the same as the average performance of the model (Koch et al., 1985), the decrease of the minimum SLP to 1017 mb and the significant reduction of the bias in the SLP to 0.1 mb at 00Z/19 represent a marked improvement over the other simulations, as will be discussed in section 4.

From the statistical scores listed in Table 2, it appears that the inclusion of sensible heating in the oceanic PBL has a significant positive effect on the model simulation of the Presidents' Day cyclone at the early stage of development, while latent heating alone yields little improvement over the ADB simulation. The remarkable improvement in the statistical scores in the BLYR NO LHT simulation for T and Td near the 1000 mb level points to the ability of surface fluxes to influence the low-level temperature and moisture structure for this case, where the overlying air mass was significantly colder than the sea surface temperature (as emphasized by Bosart, 1981; Chou and Atlas, 1982). However, the detailed diagnostic analyses which follow illustrate that the statistical results taken alone can be misleading, and that the interaction of large-scale dynamical processes (associated with the STJ), sensible and latent heat flux in the oceanic PBL, *and* latent heat release must all be incorporated to improve the model simulation of the LLJ and secondary cyclogenesis for this case. A description of the model simulations follows.

4. Description of model simulations

This section provides descriptions of the upper-level (332 K) and lower-level (292 K) winds and sea-level pressure for the adiabatic control simulation (ADB), the simulation including PBL processes only (BLYR

ADB

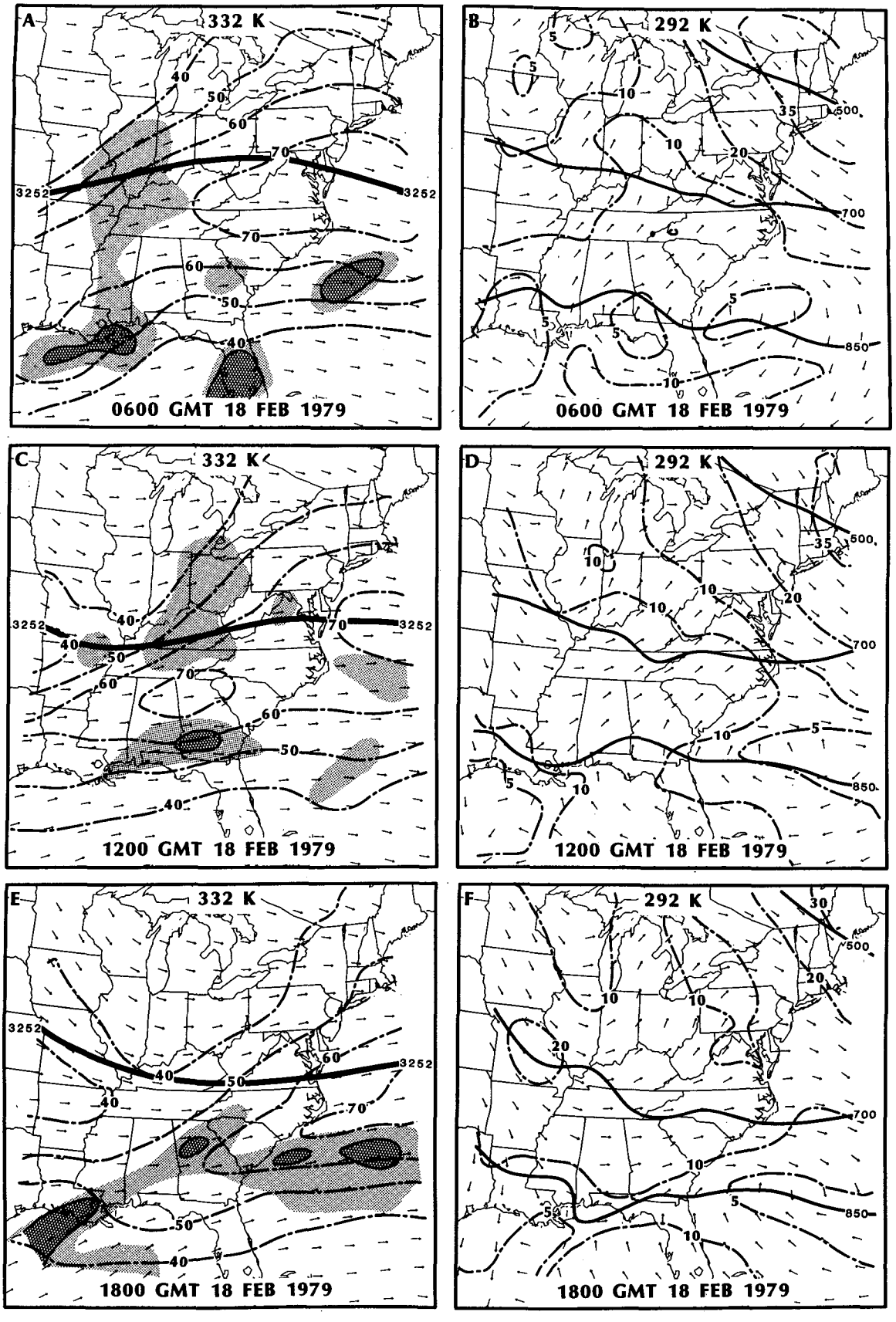
A
332 K
3252
40
50
60
70
3252
70
60
50
40
0600 GMT 18 FEB 1979
B
292 K
5
5
10
35
500
10
20
700
5
5
5
850
10
0600 GMT 18 FEB 1979
C
332 K
3252
40
40
50
70
3252
60
70
60
50
40
1200 GMT 18 FEB 1979
D
292 K
10
35
500
10
10
20
700
10
5
5
10
850
1200 GMT 18 FEB 1979
E
332 K
3252
40
60
3252
40
50
70
50
40
1800 GMT 18 FEB 1979
F
292 K
30
500
10
10
20
20
700
10
5
5
850
10
1800 GMT 18 FEB 1979

TABLE 3. Listing for upper-level trajectory A initialized at 30° latitude, 106° longitude at 0000 UTC 18 February from adiabatic experiment (ADB) (Fig. 7) and from the full physics experiment (FULL PHYS). Wind direction and speeds are in degrees and m s^{-1}, respectively (325 30 = 325°, 30 m s^{-1}), for the total horizontal vector wind (U), geostrophic wind (U_g), and ageostrophic wind (U_{ag}). Pressure (p) is in mb.

	Upper-level trajectory A from ADB				Upper-level trajectory A from FULL PHYS			
Hour	U	U_g	U_{ag}	p	U	U_g	U_{ag}	p
			First period of parcel acceleration					
01Z/18	239 52	251 52	157 10	230	239 52	250 52	159 10	231
02Z/18	242 55	247 58	141 4	231	242 55	246 56	135 4	232
03Z/18	245 57	251 59	139 7	237	245 56	251 58	144 7	239
04Z/18	246 59	249 64	104 6	246	246 58	247 65	84 6	247
05Z/18	248 61	254 64	130 7	240	247 60	251 64	109 7	244
			Second period of parcel acceleration					
10Z/18	254 60	257 58	198 4	242	248 60	253 54	213 8	229
11Z/18	259 62	258 55	271 7	244	252 60	267 50	213 20	229
12Z/18	264 63	275 55	214 14	238	258 67	272 57	209 18	225
13Z/18	269 66	275 60	225 8	230	267 71	285 53	228 26	218
14Z/18	273 67	279 70	163 8	230	274 75	286 59	237 21	224
15Z/18	276 70	279 71	176 5	237	281 77	286 64	256 14	226

NO LHT), the simulation with latent heating included but no PBL processes (LHT NO BLYR), and the simulation including PBL processes and latent heat fluxes in the PBL and latent heating (FULL PHYS). Since the formation of the LLJ near the 850 mb level is central to this study and since diabatic processes can affect the vertical position of isentropic surfaces, the 850 mb wind and temperature analyses from each simulation are also discussed to highlight differences in the lower-tropospheric wind and temperature fields.

a. Adiabatic simulation (ADB)

In ADB, the axis of the 60 and 70 m s^{-1} contours on the 332 K level (which represents the STJ located between the trough and ridge axes in Figs. 6a, 6c, and 6e) shifts southeastward with time and extends from Georgia to the Carolina coast by 18Z/18. While this southward shift in the axis of the STJ is consistent with observations (Uccellini et al., 1984), there is no appreciable increase in the total wind speed along the axis as was observed. As the region of maximum wind speeds becomes established along the East Coast, the flow becomes directed toward lower ψ_m values over the Carolinas and Virginia, with a 10 to 15 m s^{-1} south-to-southwest ageostrophic component developing over the Appalachians by 12Z/18 (see ageostrophic component for adiabatic parcel at 12Z/18 in Table 3). In association with the increasing cross-contour flow, an area of divergence greater than 2×10^{-5} s^{-1} at the 200 mb level (near the 332 K surface in the eastern United States) also develops near the ridge axis over Virginia between 06Z/18 and 12Z/18 (Fig. 6c).

Upper-tropospheric trajectories[4] computed from ADB (Fig. 7) indicate that parcels located initially along the axis of the STJ undergo two periods of acceleration, the first over Texas in the entrance region of the STJ and the second over the Appalachian region. The second acceleration occurs as the parcels approach the upper-level ridge over the Middle Atlantic states between 10Z/18 and 12Z/18 and the 200 mb divergence increases near the ridge crest over northern Virginia (Figs. 6a, 6c, and 6e). These model results indicate that the adiabatic-dynamic processes associated with the colocation of the STJ axis and ridge appear to contribute to the increasing divergence aloft between 00Z/18 and 12Z/18, as diagnosed from observed data by Uccellini et al. (1984).

Vertical cross sections constructed along a rhumb line from central Michigan to a position off the Florida coast show that an indirect transverse circulation develops in ADB between 06Z/18 and 12Z/18 on the anticyclonic side of the STJ (Fig. 8) with characteristics

[4] Trajectories are computed after completion of a simulation using the predicted u, v, and ω output at 15 min intervals. All diagnosed and predicted quantities are interpolated from the model grid to the parcel position by overlapping quadratic polynomials (horizontally) and by linear variation in σ (vertically), with the exception that temperature is vertically interpolated linearly with respect to $\ln(p)$. New parcel positions are computed by an iterative forward time step using averaged velocity components at its present and projected positions.

FIG. 6. The 6, 12, and 18 h forecasts of 332 K (left) and 292 K (right) isentropic surfaces from the adiabatic simulation (ADB) initialized at 0000 UTC 18 February 1979. The 332 K analyses (a, c, e) include wind direction (arrows), isotach (m s^{-1}, dot-dashed), and one selected ψ_m contour (solid, 3252 = 3.252×10^5 m^2 s^{-2}). Light shading indicates 200 mb divergence greater than 2×10^{-5} s^{-1}, with cross-hatched shading greater than 4×10^{-5} s^{-1}. The 292 K analyses (b, d, f) include wind direction (arrows), isotach (m s^{-1}, dot-dashed), and selected isobars (mb, solid).

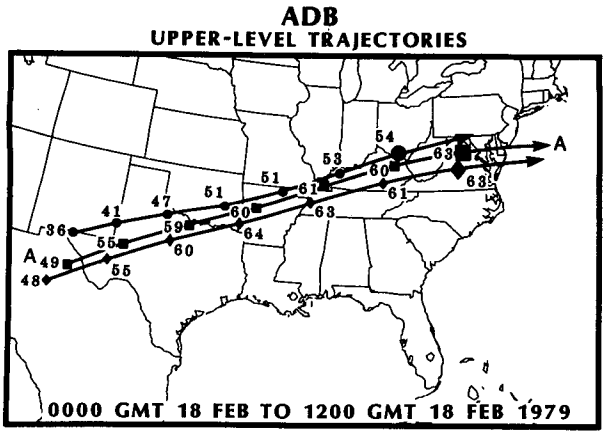

FIG. 7. Upper-level trajectories initialized at 0000 UTC 18 February 1979 from the adiabatic simulation (ADB) near 225 mb. Parcel location and wind speeds (m s^{-1}) indicated at two-hour intervals with positions at 12Z/18 represented by enlarged symbols for each trajectory. Total, geostrophic, and ageostrophic winds and pressure for trajectory A listed in Table 3.

that are similar to the indirect circulation derived from the actual data (Fig. 4). The circulation evolves from a general pattern of ascent within the plane of the cross section at 06Z/18 (Fig. 8a) to a more organized indirect circulation located over the Southeast Coast by 12Z/18 (Fig. 8b). The maximum ascent is located beneath the axis of the STJ and a distinct ageostrophic lower branch is directed from the Atlantic Ocean toward the Appalachian Mountains. However, the magnitude of the lower-tropospheric ageostrophic branch of the indirect circulation approaches a value of 13 m s^{-1}, which is slightly less than the 15 m s^{-1} value diagnosed from the coarse-resolution radiosonde data (Fig. 4). The upward vertical branch under the axis of the STJ is also small, attaining a maximum value of -5 μb s^{-1} compared to a value of -8 μb s^{-1} derived from the radiosonde database. Therefore, although the adiabatic control simulation produces an indirect circulation on the anticyclonic side of the STJ, the magnitudes of the lateral and vertical components of the circulation within the mesoscale model are less than those diagnosed from the coarse radiosonde database. Furthermore, the strong vertical gradient in the lower-tropospheric isentropes east of the Appalachian Mountains and over the ocean reflects the maintenance of very cold, stable air off the Southeast Coast with no indication of cold air damming or coastal frontogenesis in ADB.

The effect of the reduced magnitude of the indirect circulation is also evident in the evolution of the 292

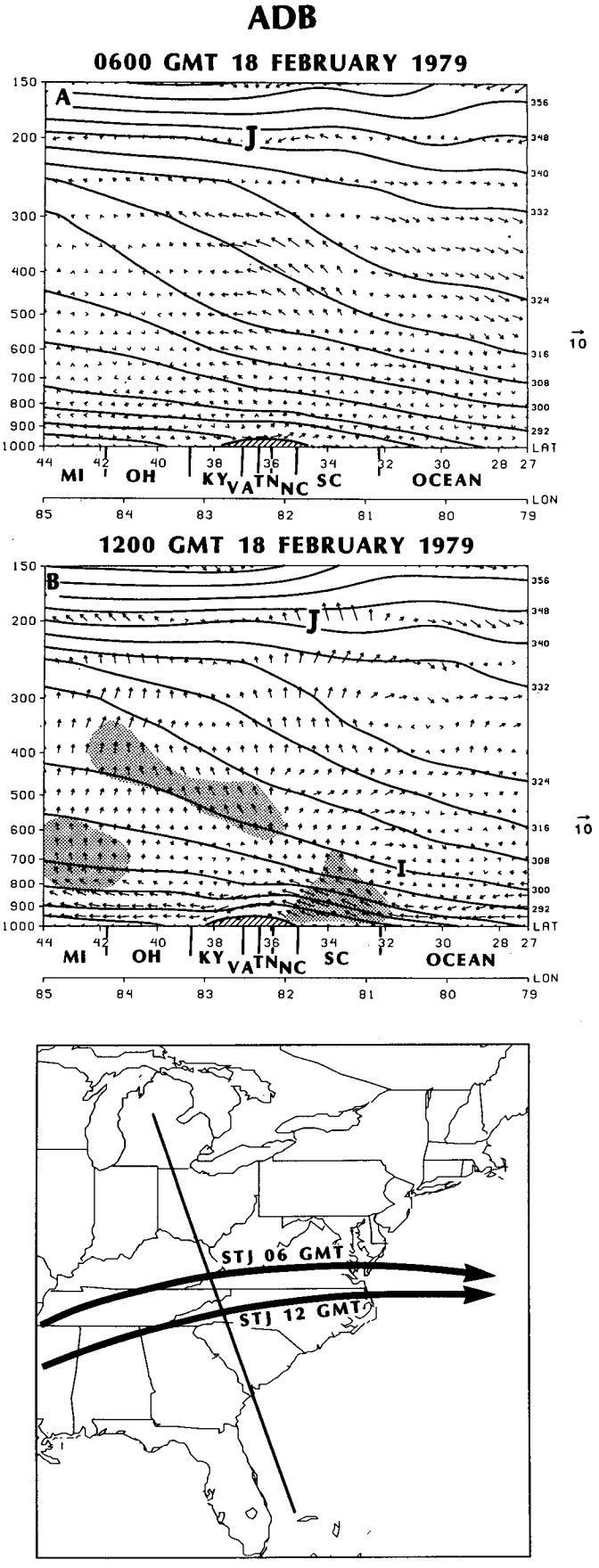

FIG. 8. Vertical cross sections of transverse ageostrophic component, vertical velocity, and potential temperature derived from the adiabatic simulation (ADB) and interpolated to vertical plane located along a rhumb line intersecting the subtropical jet (map inset): (a) 0600 and (b) 1200 UTC 18 February. See caption in Fig. 4 for details, except that shading indicates the region where ascent is greater than -4 μb s^{-1}.

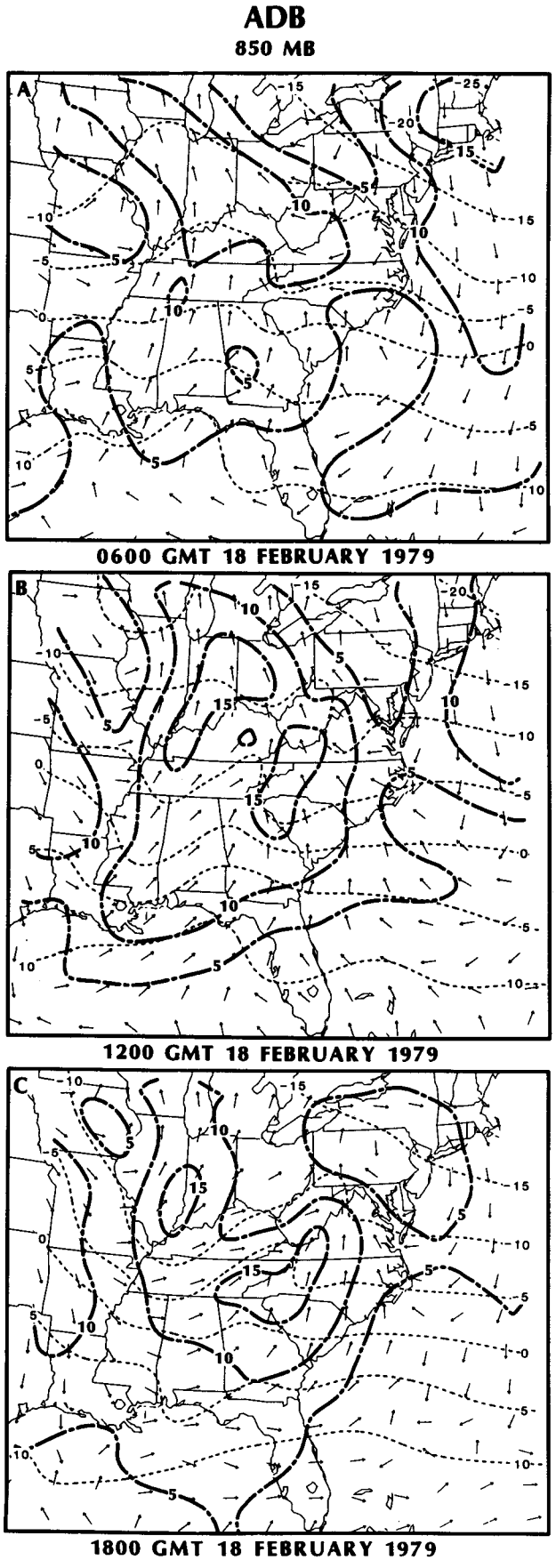

K wind fields along the East Coast from 06Z/18 to 18Z/18 (Figs. 6b, 6d, and 6f). The wind speeds over South Carolina increase to only 15 m s^{-1} by 12Z/18, a value which is 10 m s^{-1} less than observed. Furthermore, the wind direction along the Southeast Coast remains from the southwest (Fig. 6d) rather than from the southeast (Fig. 2d). Instead of a distinct, sloping wind maximum along the coast at 12Z/18, the adiabatic simulation yields a 15 to 18 m s^{-1} southwesterly wind maximum directed up the sloping isentropic surface toward the 700 mb level over Mississippi, Tennessee, and Alabama (Fig. 6d), which was not observed (Fig. 2d). The ascending flow associated with this simulated feature could be contributing to the rising branch of the indirect circulation near the 700 mb level (Fig. 8b).

The lack of agreement on the 292 K surface between ADB and observations can be attributed, in part, to the fact that without sensible and latent heating in ADB, the 292 K surface remains above the 850 mb level along the South Carolina and Georgia coasts (Fig. 6b), compared to the 850 to 900 mb level observed (Fig. 2d). Since the lower branch of the simulated indirect circulation is confined below 292 K, an increase in the low-level wind field is more evident at and below the 850 mb level for this simulation. Between 00Z/18 and 12Z/18, a 10 to 15 m s^{-1} southeasterly wind develops at 850 mb from the Carolina coast to the Appalachian Mountains (Figs. 9a and 9b). The trajectory results in section 5 reveal that the maximum wind in the lower branch of the indirect circulation in ADB approaches 20 m s^{-1} in a layer between 930 and 875 mb (see Table 5). Associated with this wind maximum, significant warm air advection develops from Alabama to North Carolina by 12Z/18 (Fig. 9b) with ascent of -4 to -6 μb s^{-1} also located over this region (not shown). However, by 18Z/18, the low-level winds decrease in magnitude along the Georgia and South Carolina coasts (as illustrated for the 850 mb level in Fig. 9c), reducing the warm air advection and associated ascent to near -2 μb s^{-1} (not shown).

With the maintenance of very cold and stable air in the lower troposphere off the East Coast, the ADB simulation produces a SLP pattern (Fig. 10) that is significantly different from that observed (Fig. 1). Only a very weak inverted trough is predicted along the East Coast by 12Z/18 in ADB (Fig. 10b). By 18Z/18, this inverted trough remains weak, while the inverted trough in the Ohio Valley slowly progresses northward. There is no indication of a coastal front in ADB as the extremely cold (and unmodified) air mass simply drifts southward behind an east-to-west frontal zone extending across Florida (Fig. 10c). Thus, while an increase in upper-level divergence over the Middle Atlantic states is simulated along an axis of a STJ between 00Z/

FIG. 9. The 850 mb wind direction (arrows), isotach (dot-dashed, m s^{-1}), and temperature (dashed, °C) analyses for the adiabatic simulation (ADB): (a) 6 h, (b) 12 h, and (c) 18 h forecasts.

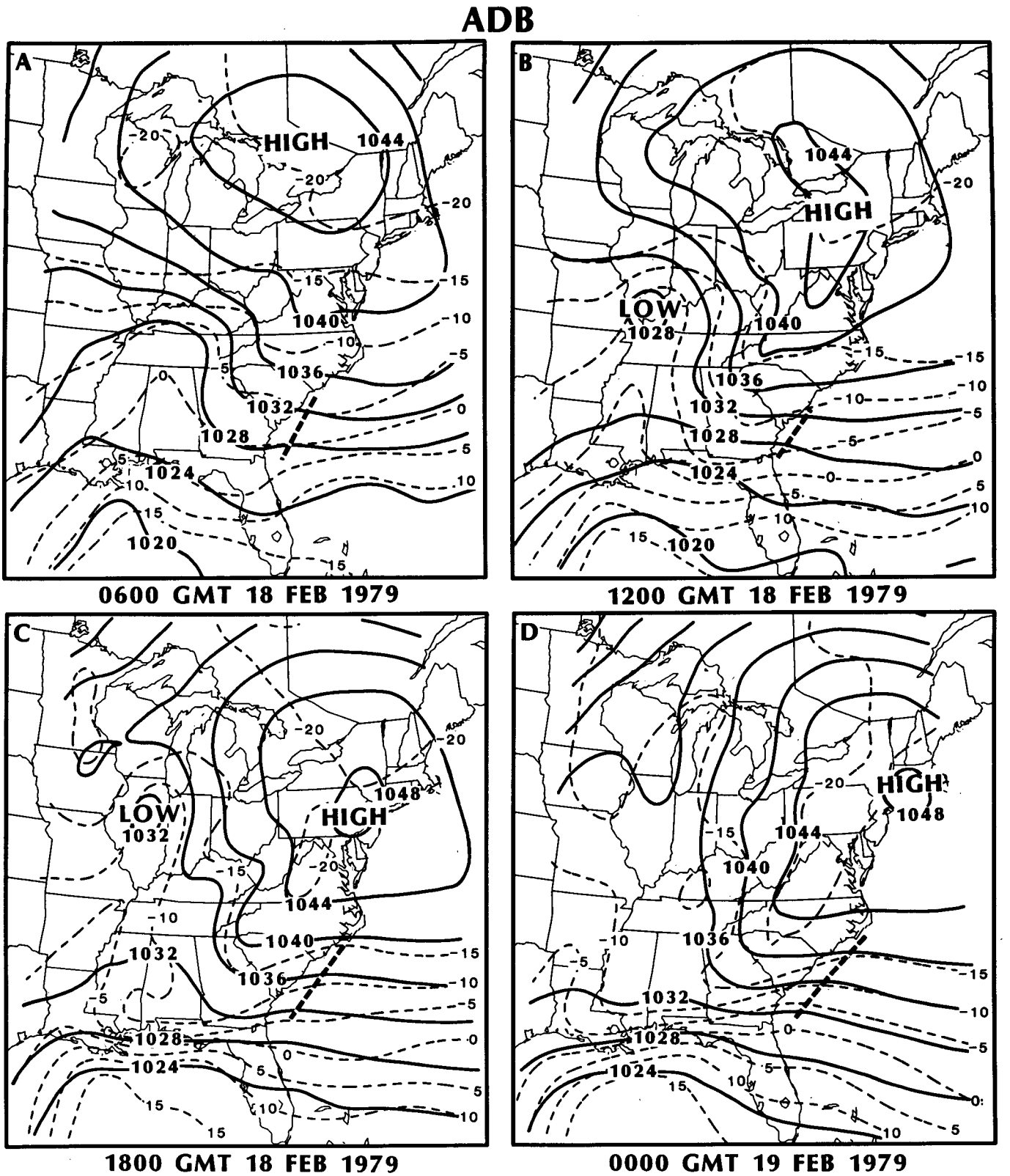

FIG. 10. Sea-level pressure (solid, mb) and isotherm (dashed, °C) analyses for the lowest model level (near 1000 mb) derived from the adiabatic simulation (ADB): (a) 6 h, (b) 12 h, (c) 18 h, and (d) 24 h forecasts. Thick dashed line represents inverted sea-level pressure trough.

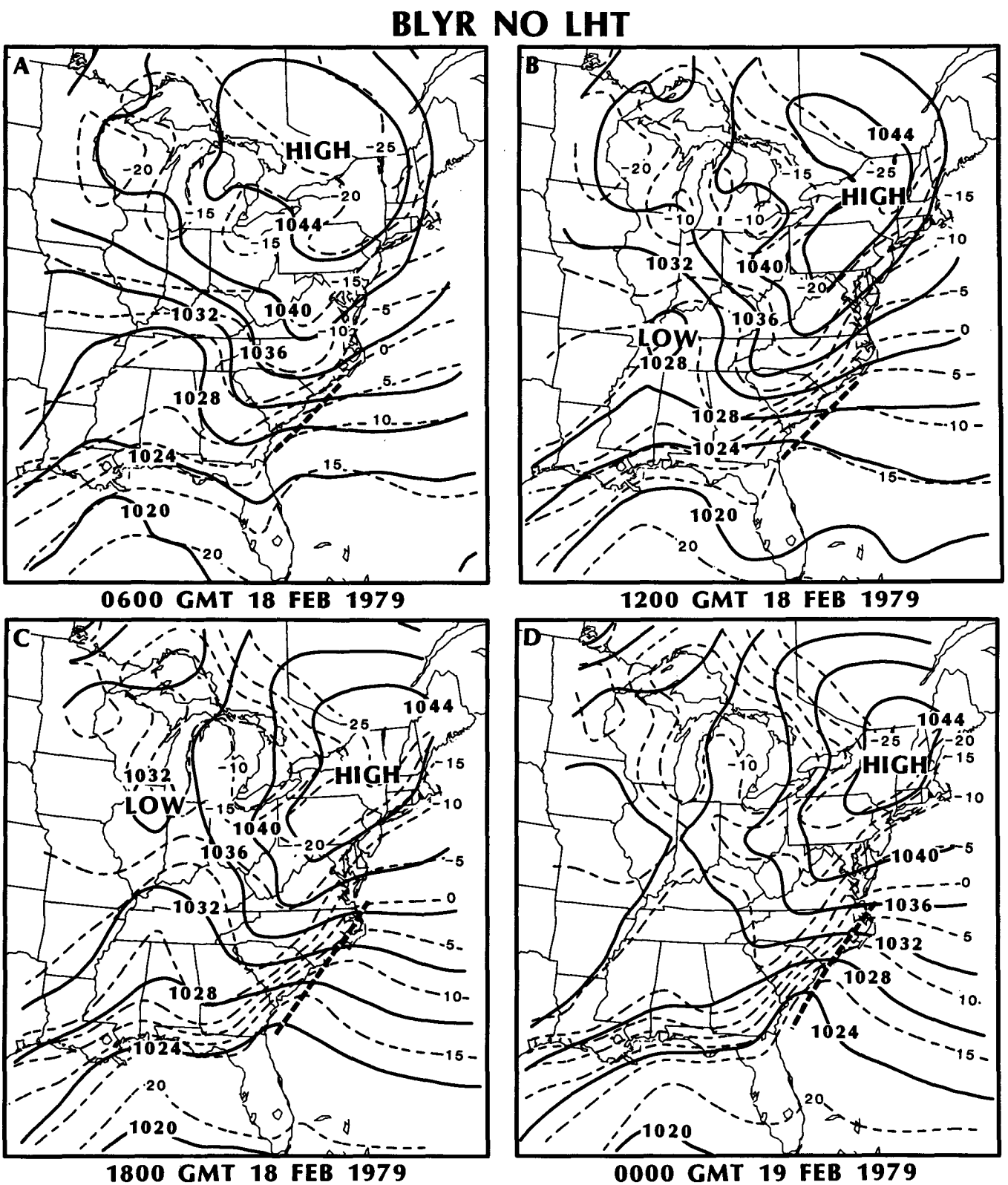

FIG. 11. As in Fig. 10 but for the boundary layer simulation with no latent heat release (BLYR NO LHT).

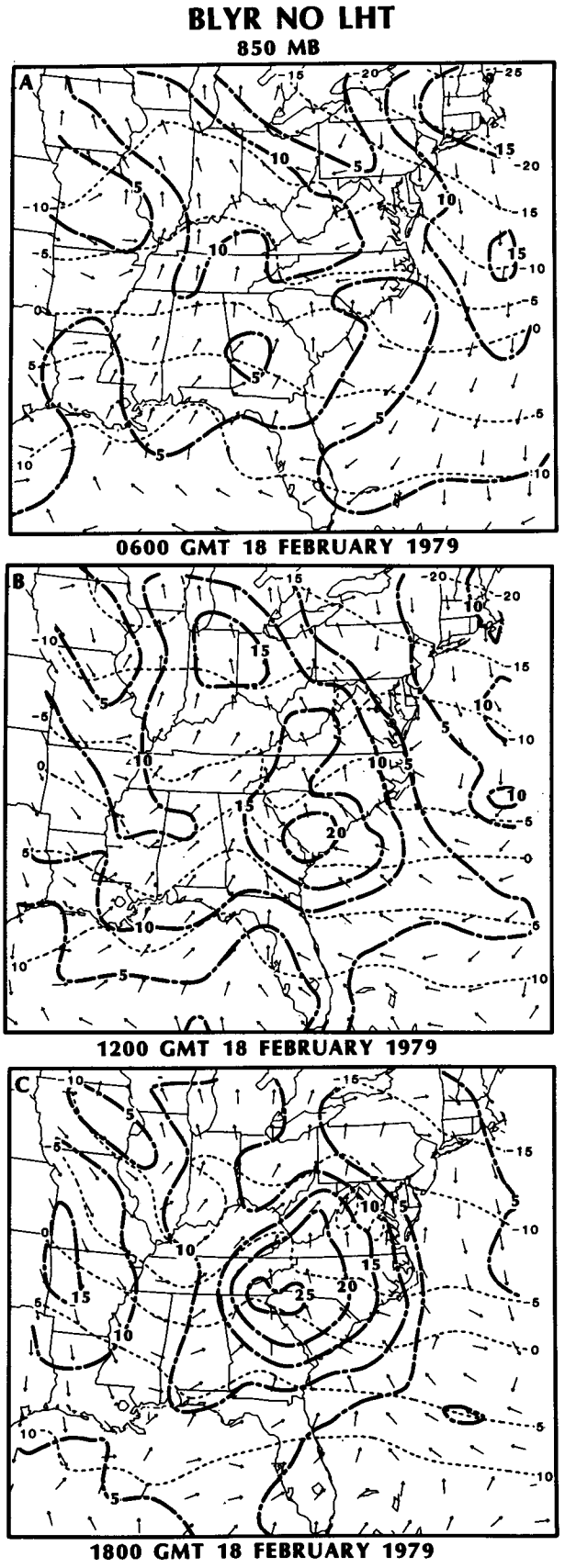

18 and 12Z/18, the response in terms of surface development is slight.

b. Boundary layer processes but no latent heat release simulation (BLYR NO LHT)

The upper-level features associated with the STJ noted in ADB are nearly the same in BLYR NO LHT and are thus not shown. However, there are significant differences in the SLP pattern and the lower-tropospheric wind fields. Between 06Z/18 and 12Z/18, a more distinct inverted trough and coastal front develop along the Southeast Coast (Figs. 11a and 11b), representing a 5 to 6 mb improvement in the SLP forecast over that predicted in ADB for the Carolina coast. The inverted trough is better defined along the coast at 18Z/18 (Fig. 11c) and 00Z/19 (Fig. 11d) compared to that predicted in ADB. However, cyclogenesis does not continue after 18Z/18 as the sea-level pressure remains nearly steady between 1024 and 1036 mb along the Carolina coastline.

The effects of sensible and latent heat fluxes in the PBL on the lower-tropospheric winds are shown in Fig. 12. The 850 mb wind becomes noticeably southeasterly and increases from 5 m s^{-1} at 06Z/18 to greater than 20 m s^{-1} at 12Z/18 just inland from the South Carolina coast. Warm air advection (and an associated -6 μb s^{-1} ascent pattern; not shown) becomes more focused along the coast between 06Z/18 and 12Z/18 (Figs. 12a and 12b). By 18Z/18, the 850 mb wind maximum, the region of warm advection, and maximum ascent shift inland to a position near the Appalachian Mountains, while the magnitudes of the wind speeds decrease along the coast with the southeasterly flow becoming parallel to the isotherms (Fig. 12c). The decrease of the warm-air advection and absence of an 850 mb thermal ridge along the coast through 18Z/18 (Fig. 12) are consistent with the lack of continued deepening of the surface system during and after this period.

As a result of the development of the inverted trough/coastal front along the coast and the continuing sensible heat release over the Atlantic Ocean, the low-level southeasterly flow just east of the Georgia–South Carolina coast yields a warm air advection pattern in the low levels which is different from that simulated in ADB. By 12Z/18, the combined effects of the warm air advection and the sensible heat flux produce 7° to 12°C temperatures on the first model level just east of the Carolina coast (Fig. 11c), compared to $-15°$ to -9°C temperatures in ADB (Fig. 10c). As noted in section 3c, the remarkable difference in the temperature forecast east of the coastline between ADB and BLYR NO LHT points to the major influence sensible heat fluxes over the ocean have on the initial development

FIG. 12. As in Fig. 9 but for the boundary layer simulation with no latent heat release (BLYR NO LHT).

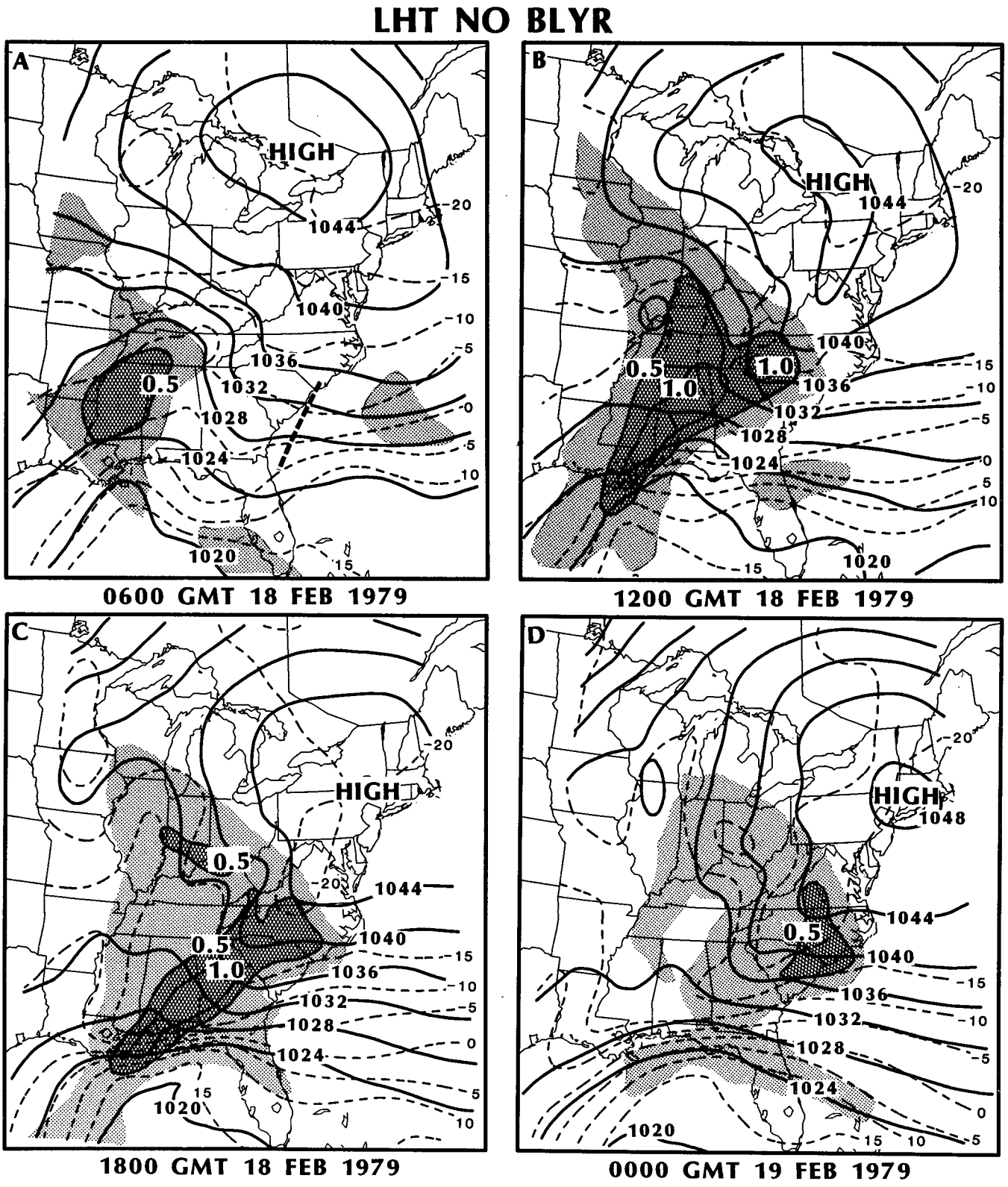

FIG. 13. Sea-level pressure (solid, mb) and isotherm analyses (dashed, °C) for the lowest model level (near 1000 mb) for simulation with latent heat and no boundary layer (LHT NO BLYR). Light shading indicates six-hourly precipitation amounts greater than 0.02 cm and vertically hatched shading indicates six-hourly precipitation greater than 0.5 and 1.0 cm. Thick dashed line represents inverted sea-level pressure trough.

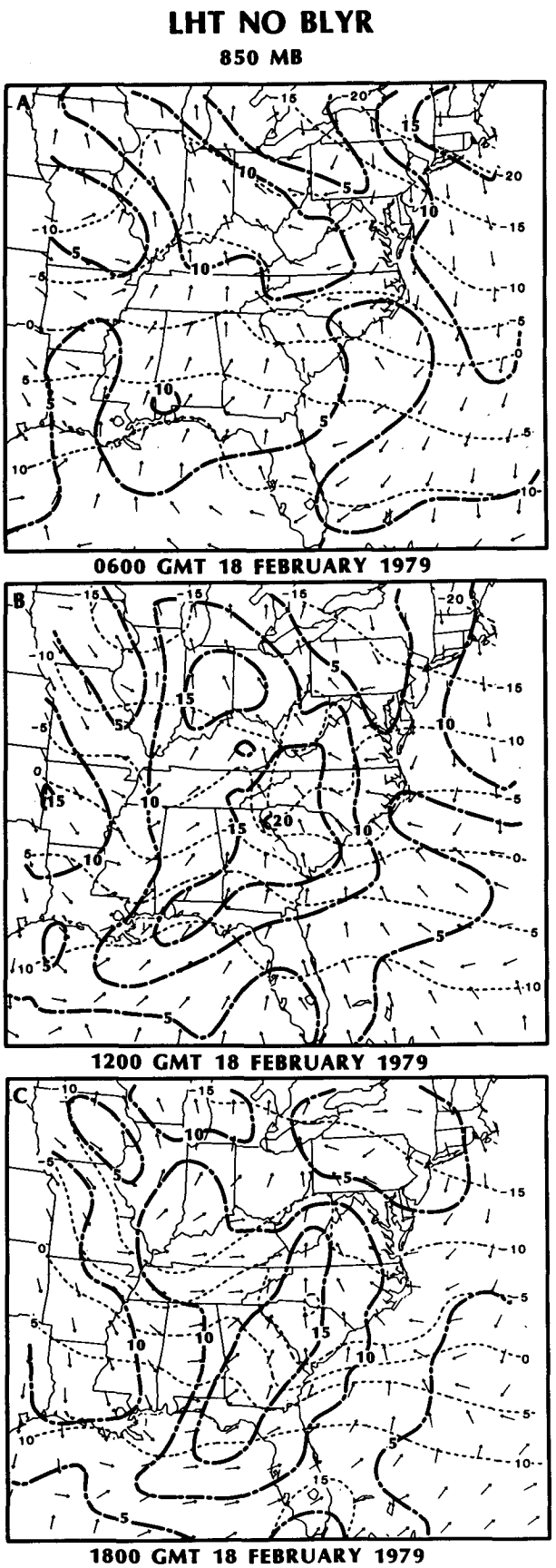

of this storm system, where the overlying air was significantly colder than the SST.

In summary, the inclusion of sensible and latent heat fluxes in the PBL yields a better simulation of the low-level wind field, coastal frontogenesis, and inverted trough by 12Z/18 and 18Z/18, but fails to produce the subsequent amplification of these features after 18Z/18 associated with the secondary cyclogenesis observed in this case.

c. *Latent heating but no boundary layer processes simulation (LHT NO BLYR)*

In LHT NO BLYR, latent heating associated with resolvable grid-scale precipitation and convective parameterization is accounted for, but sensible and latent heat fluxes in the PBL are not included. This simulation produces an area of grid-scale precipitation that is centered over Mississippi during the first 6 h (Fig. 13a). The area of precipitation extends northeastward to North and South Carolina by 12Z/18 (Fig. 13b) and to the North Carolina coast by 18Z/18 (Fig. 13c). The areal extent of the precipitation in the southeastern United States in LHT NO BLYR is consistent with the observations (see Fig. 1). However, the precipitation rates predicted in the Carolinas are less than those observed (especially between 12Z/18 and 00Z/19), reflecting the lack of a moisture flux in the oceanic PBL. The surface trough along the coast in LHT NO BLYR (Fig. 13) is again very weak, as was the case for ADB, and there is no evidence of a coastal front as the cold air along the East Coast simply moves south toward Florida.

The presence of latent heat release produces subtle but important changes in the simulation of the upper-level wind field from that shown in ADB that influence the cross-contour flow near the ridge axis and associated magnitude of the upper-level divergence. These changes are discussed in detail in sections 4d and 6. At 850 mb, a wind maximum develops over southeastern United States between 06Z/18 and 12Z/18 in LHT NO BLYR (Fig. 14) with 15 m s^{-1} southeasterly winds developing along the coast during this period. By 18Z/18, the 850 mb wind speed begins to decrease in the Carolinas and the wind direction becomes more southerly (Fig. 14c). Despite the southerly wind, the 850 mb temperatures actually decrease in the Carolinas and Georgia during the first 18 h with only a slight indication of an 850 mb thermal ridge developing along the coast, which is again consistent with the lack of surface development in this simulation. It thus appears that a continued amplification of the 850 mb wind field cannot be sustained and that the development of a thermal ridge along the coast and cyclogenesis in the southeastern United States do not occur by including latent heat of

FIG. 14. As in Fig. 9 but for simulation with latent heat release but no boundary layer physics (LHT NO BLYR).

condensation without also accounting for heat and moisture fluxes within the oceanic PBL.

d. Full physics simulation (FULL PHYS)

The most accurate simulation of the secondary surface cyclogenesis along the coast is accomplished by including the sensible and latent heat fluxes in the PBL and latent heat release. The maintenance of a distinct pressure ridge east of the Appalachian Mountains, the development of an inverted trough along the Southeast Coast and associated coastal frontogenesis, and the weakening of the Ohio Valley trough between 06Z/18 and 18Z/18 (Figs. 15a, 15b, and 15c) agree favorably

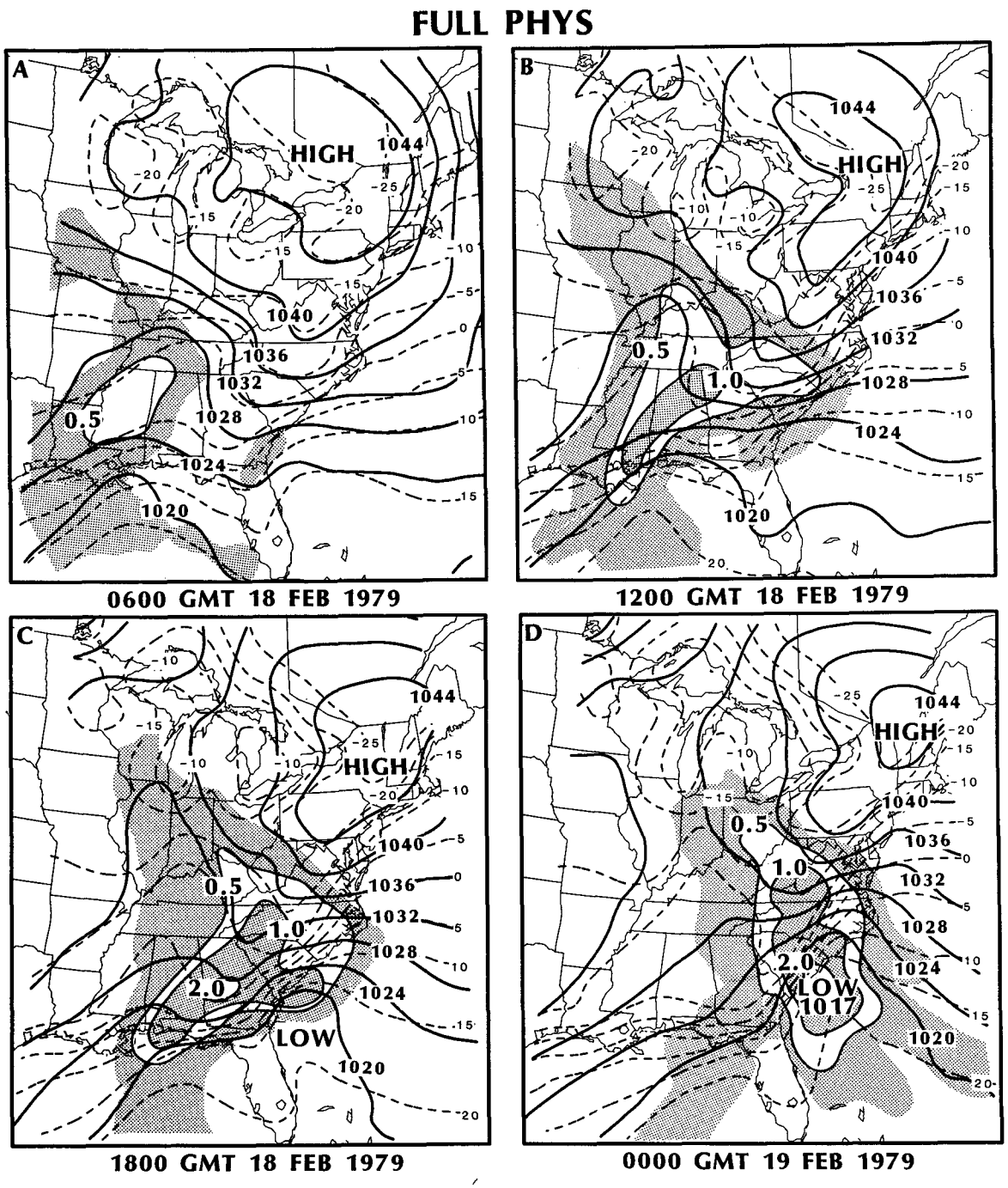

FIG. 15. Sea-level pressure (solid, mb) and isotherm analyses (dashed, °C) for lowest model level (near 1000 mb) for the full physics simulation (FULL PHYS). Alternating intervals of shading indicates six-hourly precipitation amounts greater than 0.02, 0.5, 1.0, and 2.0 cm. Thick dashed line represents inverted sea-level pressure trough.

with the analyses provided by Bosart (1981) and Uccellini et al. (1984). By 00Z/19, the coastal system continues to deepen off the South Carolina coast (Fig. 15d), with the 1017 mb central pressure identical to that analyzed by Bosart (1981). However, the axis of the inverted trough is shifted slightly inland in North Carolina compared to the observations, which could account for the S1 score of 45.6 for this simulation (see Table 2).

The precipitation produced in FULL PHYS is similar to LHT NO BLYR for the first 6 h of the simulation. However, by 12Z/18, the precipitation shield moves farther east compared to LHT NO BLYR, extending east of the coastline (compare Figs. 13b and 15b). The eastward expansion and increasing amounts of precipitation indicate that the moisture and heat fluxes within the oceanic PBL act to fuel the developing area of precipitation between 06Z/18 and 12Z/18 (as can be seen by comparing the mixing ratio listed for the ADB and FULL PHYS low-level trajectories in Table 5). By 18Z/18 and 00Z/19, significant precipitation continues to move northeastward into Virginia, with lighter precipitation extending northwestward into the Ohio Valley (Figs. 15c and 15d).

The combined effects of the ocean-influenced PBL and latent heat release alter the mass and wind fields throughout the entire troposphere. At 12Z/18, the magnitude of the 332 K winds along the axis of the STJ is slightly larger than ADB over the Middle Atlantic coast (compare Figs. 16c and 6c), although the wind speed is still 5 to 10 m s^{-1} less than observed over the Carolinas.[5] There are other differences between ADB and FULL PHYS. First, the 332 K ridge axis over West Virginia in FULL PHYS (Fig. 16c) is displaced approximately 200 km to the west of the position of the ridge axis in ADB (Fig. 6c). Furthermore, the cross-contour ageostrophic flow near the ridge axis over Virginia is larger in FULL PHYS (as revealed by the trajectory computations discussed below). In conjunction with the increased cross-contour flow along the axis of the STJ, the upper-level divergence is significantly larger over the Appalachian region at 12Z/18 in FULL PHYS than in ADB (compare Figs. 16c and 6c). The upper-level divergence then shifts southeastward and decreases in magnitude by 18Z/18 (Fig. 16e). This is consistent with the satellite imagery for this case, which shows that the areal extent of the clouds actually decreases after 12Z/18 as the first area of precipitation progresses eastward (Uccellini et al., 1984).

Upper-tropospheric trajectories derived from FULL PHYS move along very similar paths as in ADB (Fig. 7) and are thus not shown. However, the trajectories from FULL PHYS develop a 20 m s^{-1} ageostrophic component ($\mathbf{U}_{ag}$) by 11Z/18 and 26 m s^{-1} by 13Z/18 compared to 14 and 8 m s^{-1}, respectively, for the ADB trajectory (Table 3). Furthermore, $\mathbf{U}_{ag}$ in FULL PHYS is directed 40° to 61° to the left of the geostrophic component ($\mathbf{U}_g$) between 10Z/18 and 12Z/18, indicating that the parcel trajectory is directed toward lower ψ values during this period (Table 3). In association with the larger $\mathbf{U}_{ag}$, the wind speed for the FULL PHYS parcel increases by more than 12 m s^{-1} between 11Z/18 and 14Z/18, compared to a 5 m s^{-1} increase during the same 3 h period for parcel A in ADB. The FULL PHYS parcel accelerates as it rises to the 218 mb level and crosses the ridge axis, as defined by the change in the direction of $\mathbf{U}_g$ from 253° at 10Z/18 to 286° at 14Z/18 (Table 3). The larger cross-contour ageostrophic component is also consistent with the larger divergence diagnosed at the 200 mb level in FULL PHYS (Fig. 16c) compared to ADB (Fig. 6c). The model trajectory from FULL PHYS closely resembles the diagnostic trajectory computed from radiosonde data for this case (shown in Fig. 11 and Table 1 in Uccellini et al., 1984). This favorable comparison again indicates that the increasing cross-contour ageostrophic wind component was associated with the acceleration of parcels through the ridge crest and the increasing divergence aloft at 12Z/18.

A vertical cross section constructed at a significant angle to the axis of the STJ (identical to the line used in Fig. 8) shows that, in conjunction with the larger upper-level divergence in FULL PHYS, a more intense indirect circulation is diagnosed on the anticyclonic side of the STJ by 12Z/18 (Fig. 17). By 06Z/18, the transverse circulation is detectable over the Appalachian Mountain region, with a 6 μb s^{-1} ascending branch located beneath the axis of the STJ (Fig. 17a). By 12Z/18, the indirect circulation is better defined and shifted farther eastward and centered near the South Carolina coastline on the anticyclonic side of the STJ (Fig. 17b), which is in general agreement with the observed circulation (Fig. 4). The ascent maximum beneath the axis of the STJ has increased to -12 μb s^{-1} at 12Z/18 compared to -5 μb s^{-1} in ADB (Fig. 8b). These results are consistent with Cahir's (1971) model experiments, which demonstrate that diabatic processes can double the magnitude of ascending branches of transverse circulations associated with jet streaks. The horizontal branches of the indirect circulations for FULL PHYS are also larger than those diagnosed for ADB, especially in the lower troposphere where ageostrophic wind components that define the lower branch of the indirect circulation now exceed 15 to 20 m s^{-1} near the 850 mb level at 12Z/18 (Fig. 17b) compared to the 10 to 15 m s^{-1} values in ADB (Fig. 8b). The cross sections from FULL PHYS also depict the ageostrophic component directed to the left of the flow above 400 mb on the cyclonic side of the STJ, which is consistent with the observed cross section (Fig. 4) and the parcel accelerations in this region. It appears

[5] As noted by Uccellini et al. (1984, p. 35), the radiosonde-based observations of 80 to 85 m s^{-1} wind speeds in the core of the STJ may contain errors related to the low elevation angle associated with measuring large wind speeds in the upper troposphere.

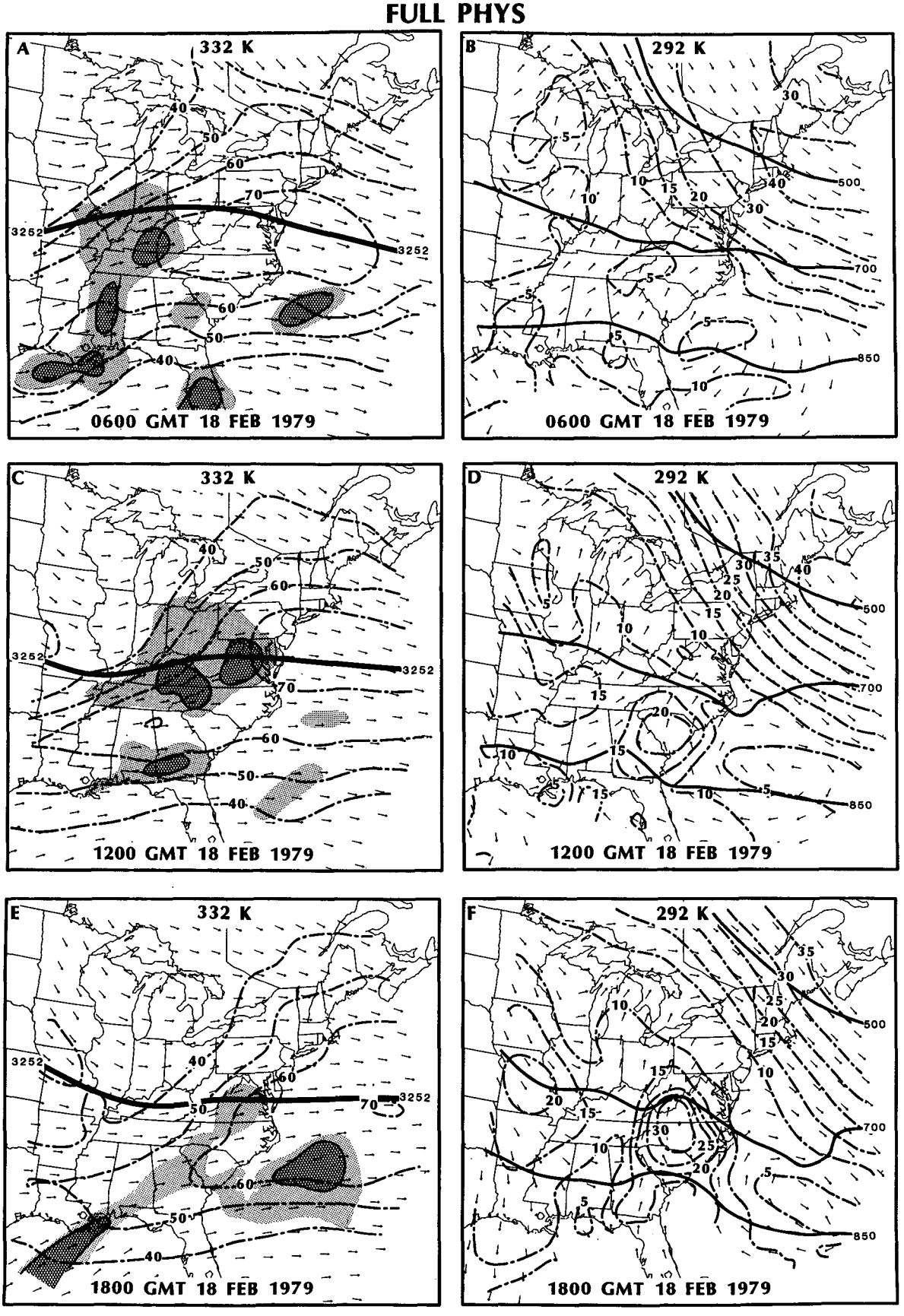

FIG. 16. The 6, 12, and 18 h forecasts of 332 K (left) and 292 K (right) isentropic surfaces from the full physics simulation (FULL PHYS) initialized at 0000 UTC 18 February 1979. See Fig. 6 caption for details.

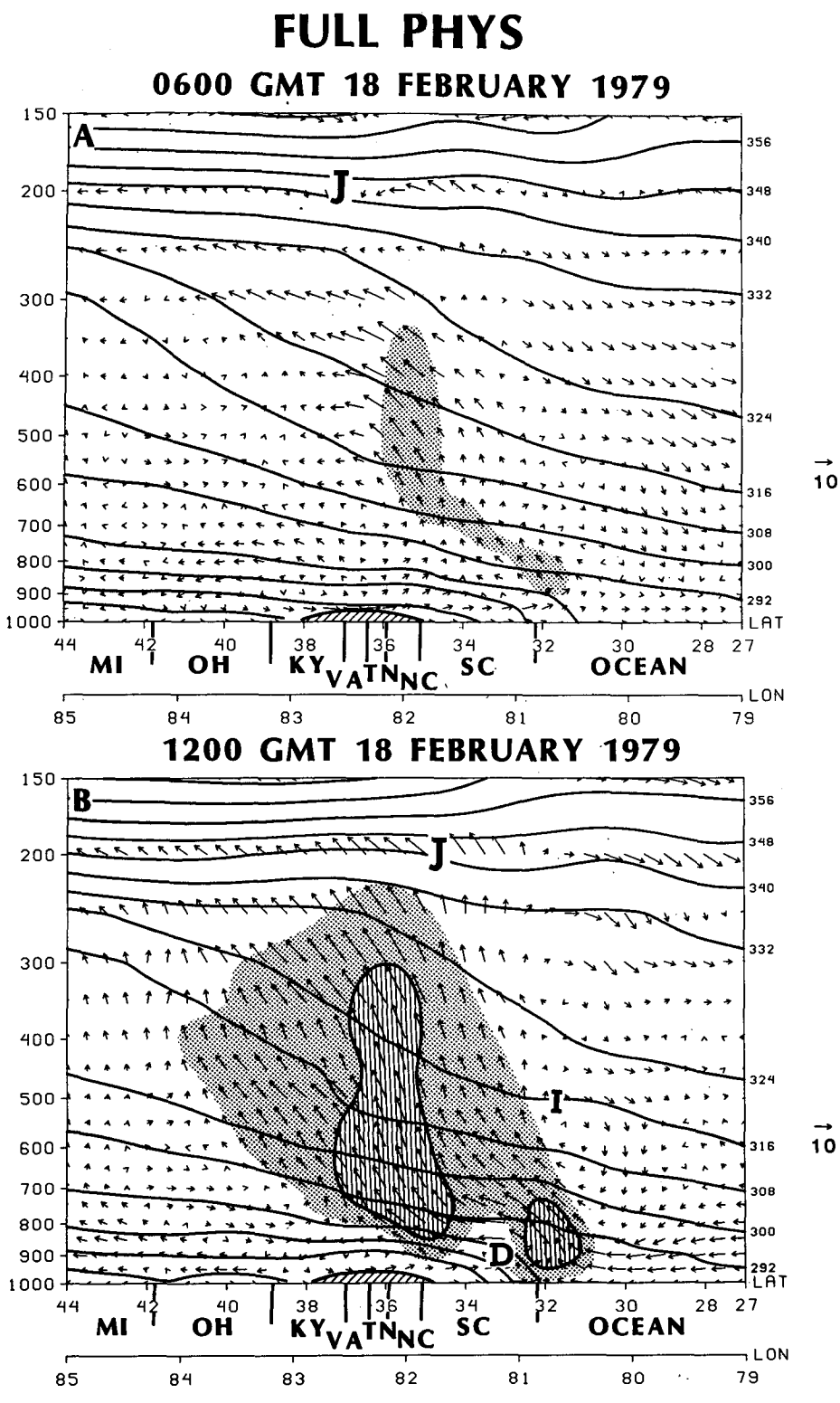

FIG. 17. Vertical cross sections from full physics simulation (FULL PHYS) along line shown in map inset used for Fig. 8. See Fig. 4 caption for details, except that light and vertical shading indicate regions where ascent is greater than -4 and -8 μb s^{-1}, respectively. *D* in (b) refers to the direct circulation associated with coastal frontogenesis.

that this component (as well as that directed into the plane of the cross section) could be contributing to the upper-level divergence along the axis of the STJ.[6]

The vertical cross sections constructed for FULL PHYS at 06Z/18 and 12Z/18 (Figs. 17a and 17b) also reveal the distinct frontogenesis along the coastline (reflected by the tightening of the gradient of potential temperature immediately along the coast in the plane of the cross section), which does not appear in the ADB cross sections (Fig. 8). Associated with the coastal frontogenesis is a shallow direct circulation (indicated by a "D" in Fig. 17b), which is marked by a separate ascent maximum in the warmer air to the east of the coastal front and descent (especially near 900 mb) in the colder air to the west. The ascent maximum near the coastal front exceeds -10 μb s^{-1} and likely contributes to the eastward extension of the precipitation shield to the coast by 12Z/18 in FULL PHYS (Fig. 15b). The upper horizontal branch of the direct circulation associated with the coastal front also appears to merge with the lower horizontal branch of the indirect circulation associated with the STJ near the 850 mb level.

The greater magnitude of the lower branch of the indirect circulation in FULL PHYS is apparent in the 292 K wind field in the southeastern United States. Between 06Z/18 and 12Z/18, wind speeds increase from 10 m s^{-1} to greater than 20 m s^{-1} over South Carolina, with the wind directed from the southeast over the Carolina coast (Figs. 16b and 16d). By 14Z/18 (not shown), the 292 K surface descends to a pressure near the 850 mb level along the coast and wind speeds continue to increase on the isentropic surface, exceeding 30 m s^{-1} over South and North Carolina by 18Z/18 (Fig. 16f). The 292 K analyses from FULL PHYS illustrate that a southeasterly LLJ develops very rapidly and extends up a sloping isentropic surface from below 850 mb off the Carolina coast to above the 700 mb level over southwestern Virginia. Furthermore, only in FULL PHYS is the LLJ maintained through 18Z/18 east of the Appalachian Mountains. The rapid development of the LLJ, as depicted on the 850 mb surface, is described in more detail in section 5 and its apparent contribution to the early stages of cyclogenesis along the coast discussed in section 6.

e. *Summary of model simulations*

The adiabatic simulation produces upper-level divergence along the axis of the STJ and an indirect circulation displaced to the anticyclonic side of the jet streak. However, the magnitudes of the horizontal and vertical components of this circulation are less than those diagnosed from observations, especially the lower-tropospheric horizontal component. Furthermore, the development of an inverted trough and associated coastal front remains weak in the adiabatic simulation. As indicated in Table 4, the separate inclusion of *either* diabatic processes associated with an ocean-influenced PBL *or* latent heat of condensation leads to an increase in the lower-tropospheric wind between 06Z/18 and 12Z/18 and decrease in the minimum SLP. However, the separate contributions are not sufficient by themselves to yield a LLJ of sufficient magnitude or surface low along the coast that satisfactorily matches the observations. Although the separate inclusion of sensible heating yields a coastal front and modest inverted trough, it is not sufficient to ensure the continual development of the secondary cyclone after 18Z/18. Yet, without the contributions of the moisture and heat flux in the oceanic boundary layer to the developing precipitation region, the latent heat of condensation is also not sufficient to amplify the lower-tropospheric wind fields to the observed levels, nor to produce the development of an inverted trough and surface low along the coast. Table 4 shows that the difference in the maximum 850 mb wind speed between ADB and FULL PHYS at 12Z/18 (13 m s^{-1}) cannot be accounted for by simply adding the difference between BLYR NO LHT and ADB (6 m s^{-1}) and the difference between LHT NO BLYR and ADB (3 m s^{-1}). Likewise, the difference in SLP at 00Z/19 between the ADB and FULL PHYS (19 mb) cannot be accounted for by adding the difference between BLYR NO LHT and ADB (12 mb) and the difference between LHT NO BLYR and ADB (0 mb). *These results demonstrate that the LLJ, secondary cyclogenesis, and the coastal front can only be properly simulated for this case when these diabatic processes interact synergistically with the dynamical processes associated with the upper-level jet.* These results are in agreement with a growing number of observational and modeling papers that discuss the importance of diabatic processes in 1) the modulation of jet streak circulations (Cahir, 1971; Kaplan et al., 1984; Kocin et al., 1986; Zack et al., 1987), 2) the formation of cyclones in general (e.g., Danard, 1964; Petersen, 1975; Gall, 1976; Johnson and Downey, 1976; Sanders and Gyakum, 1980; Chang et al., 1982; Gyakum, 1983a,b; Anthes et al., 1983), and 3) the development of storms along the east coast of the United States (Bosart, 1981; Kaplan et al., 1982b; Bosart and Lin, 1984; Zack et al., 1984; Kocin et al., 1985c; Atlas, 1987).

In the following sections, trajectory computations and model diagnostics are presented to show 1) how the jet streak–related dynamical process and diabatic processes contribute to the development of the LLJ and 2) how the parcel accelerations associated with the LLJ formation act to focus the surface pressure falls

[6] As noted by Uccellini et al. (1984, pp. 50–51), although the indirect circulation is depicted on a two-dimensional plane, three-dimensional processes (associated with the anticyclonic curvature of the flow field, decreasing wavelength between the trough and ridge axes, and diabatic processes) contribute to the development of this indirect circulation and its displacement to the anticyclonic side of the STJ for this case.

TABLE 4. Comparison of 1) maximum 850 mb wind speed (m s^{-1}) for LLJ feature in southeastern United States for 06Z/18 and 12Z/18 and 2) minimum sea-level pressure (SLP; mb) for location just off South Carolina coast for the times indicated, for the four model simulations listed in Table 2.

	Maximum 850 mb wind		Minimum SLP				
Simulation	06Z/18	12Z/18	00Z/18	06Z/18	12Z/18	18Z/18	00Z/19
ADB	5	18	1032	1032	1032	1035	1036
BLYR NO LHT	5	24	1032	1030	1027	1027	1024
LHT NO BLYR	6	21	1032	1030	1032	1036	1036
FULL PHYS	6	31	1032	1028	1024	1022	1017

along the coast, a process that constitutes the incipient development of the cyclone.

5. The development of the low-level jet

As described in section 4, the FULL PHYS simulation produces a significant LLJ that extends from below 850 mb near the coastline to above 700 mb over the Appalachian Mountains. Furthermore, it appears that the LLJ develops in the region where the lower branch of the indirect circulation (associated with the STJ) and the upper branch of the direct circulation (associated with coastal frontogenesis and damming) merge near the 850 mb level (Fig. 17b).

An hourly sequence of the 850 mb total (**U**) and ageostrophic ($\mathbf{U}_{ag}$) winds reveals that, between 06Z/18 and 09Z/18, $\mathbf{U}_{ag}$ increases dramatically along the South Carolina coast, from 9 m s^{-1} at 06Z/18, to 18 m s^{-1} at 07Z/18, to 25 m s^{-1} at 08Z/18 (not shown), to a distinct east-southeasterly, 27 m s^{-1} maximum by 09Z/18 (Fig. 18a2). This sudden enhancement in the magnitude of $\mathbf{U}_{ag}$ within 3 h is a measure of the increasingly unbalanced flow regime that develops along the coast as the simulated coastal front begins to develop.

The changes in the magnitude of **U** lag that for $\mathbf{U}_{ag}$ along the South Carolina coast, increasing from 9 m s^{-1} at 06Z/18, to 10 m s^{-1} at 07Z/18, to 16 m s^{-1} at 08Z/18 (not shown), to 19 m s^{-1} at 09Z/18 (Fig. 18a1). This lag in the response of **U** to the large values of $\mathbf{U}_{ag}$ along the coast persists through the following 3 h. The southeasterly $\mathbf{U}_{ag}$ along the South Carolina coast increases to 36 m s^{-1} at 10Z/18 (Fig. 18b2), to 39 m s^{-1} by 11Z/18 (Fig. 18c2), and finally stabilizes near 37 m s^{-1} by 12Z/18 (Fig. 18d2). The magnitude of **U** continues to increase during the entire 3 h period (Figs. 18a1, 18b1, 18c1, and 18d1), exceeding 30 m s^{-1} over western South Carolina by 12Z/18.

To isolate the processes that contribute to the development of the LLJ, a trajectory is shown for a parcel that passes through the low-level wind maximum in FULL PHYS and then compared to a parcel trajectory computed for ADB (Fig. 19). The trajectories are obtained in the following manner. A parcel near the area of the 850 mb wind maximum in South Carolina at 12Z/18 is selected to initialize the trajectory for FULL PHYS. A backward trajectory is computed for the period between 00Z/18 and 12Z/18 and a forward trajectory for the period between 12Z/18 and 18Z/18 (Fig. 19a). A similar procedure is used to initialize a trajectory for ADB that passes through a wind maximum at 875 mb in South Carolina between 10Z/18 and 12Z/18 (Fig. 19b). Both trajectories are generated in the manner described in section 4a. A breakdown of the total (**U**), geostrophic ($\mathbf{U}_g$), and ageostrophic ($\mathbf{U}_{ag}$) winds, θ, P, and the mixing ratio (q) is provided for each in Table 5.

To represent the balance of forces affecting the acceleration of parcels, $\mathbf{U}_g$, $\mathbf{U}_{ag}$, **U**, and pressure are also displayed in Fig. 19. The $\mathbf{U}_g$ vector can be used as a measure of the pressure gradient force experienced by the parcel at a given time. The $\mathbf{U}_{ag}$ vector is a measure of the imbalance between the pressure gradient and Coriolis forces, with instantaneous accelerations directed to the right of $\mathbf{U}_{ag}$.

The ADB trajectory experiences a relatively weak pressure gradient force as it propagates first toward the southwest before 06Z/18 (Fig. 19b). As the parcel approaches the coast between 06Z/18 and 10Z/18, it accelerates to 20 m s^{-1} and ascends from 934 to 911 mb. This acceleration occurs within the lower branch of the indirect circulation (depicted in Fig. 8) as the parcel maintains a $\mathbf{U}_{ag}$ directed to the left of $\mathbf{U}_g$ (Fig. 19b). The wind speed of 20 m s^{-1} at 11Z/18 represents the maximum attained by the adiabatic trajectory east of the Appalachian Mountains as the **U** vector rotates from a direction to the left of $\mathbf{U}_g$ at 08Z/18, consistent with parcel acceleration, into a direction toward the right of the geostrophic vector by 12Z/18, consistent with parcel deceleration (see Fig. 19b). The parcel decelerates after 12Z/18 and turns anticyclonically toward the north and then northeast.

The $\mathbf{U}_g$, $\mathbf{U}_{ag}$ and **U** components for the FULL PHYS trajectory (Fig. 19a) differ from its adiabatic counterpart. Between 06Z/18 and 12Z/18, **U** for the FULL PHYS parcel is directed at a significantly greater angle to the left of $\mathbf{U}_g$ and for a longer period of time than its adiabatic counterpart as the parcel ascends from 936 to 850 mb. When the parcel ascends from 921 mb at 08Z/18 to 880 mb at 10Z/18, the magnitude of $\mathbf{U}_{ag}$ increases rapidly to 28 m s^{-1} and the angle between **U**

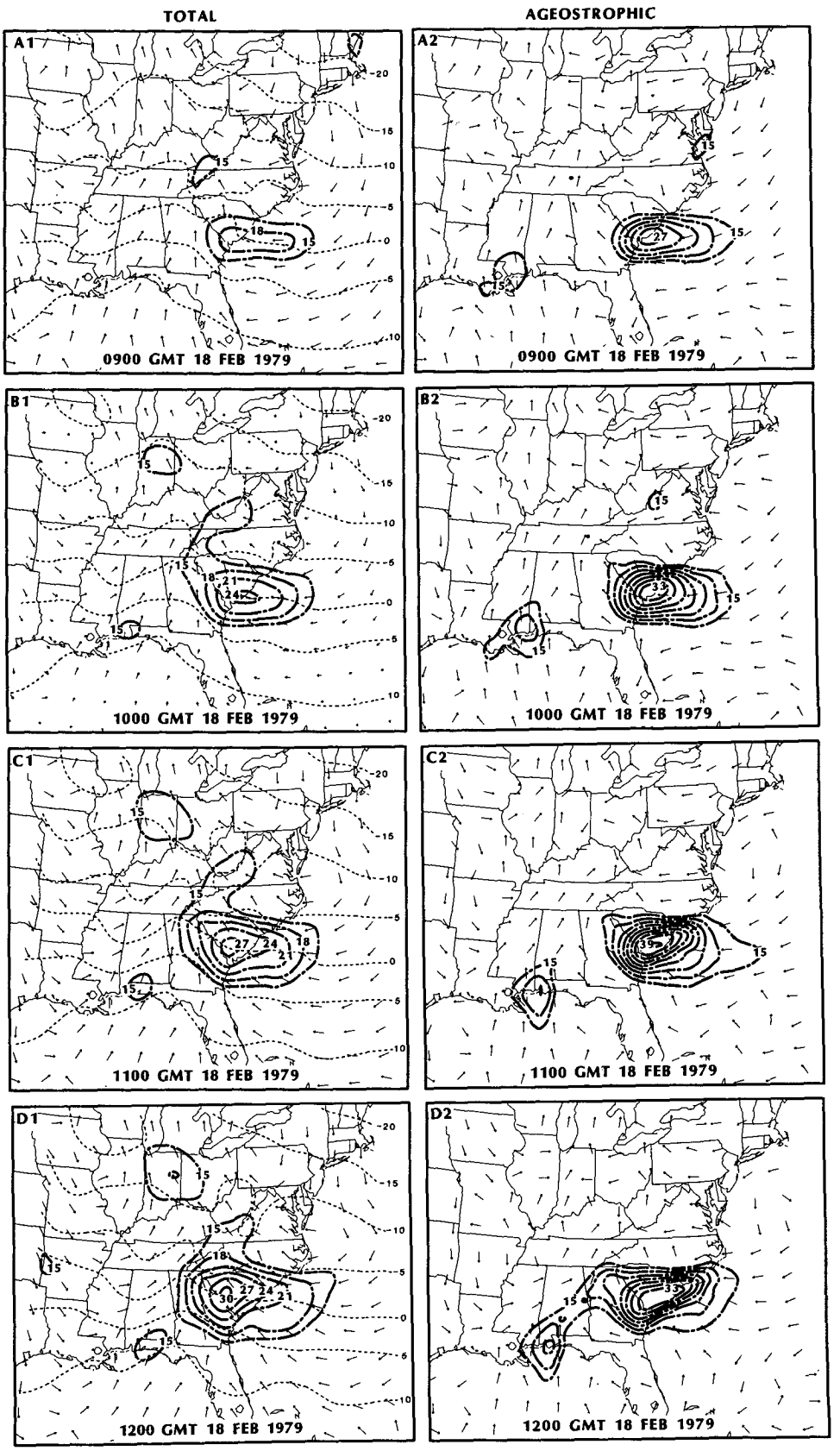

FIG. 18. Hourly sequence of 850 mb wind direction (arrows) and isotachs (dot-dashed, m s^{-1}), total wind (left column; a1, b1, c1, d1) with isotherms included (dashed, °C), and for ageostrophic wind (right column; a2, b2, c2, d2) from the full physics simulation (FULL PHYS).

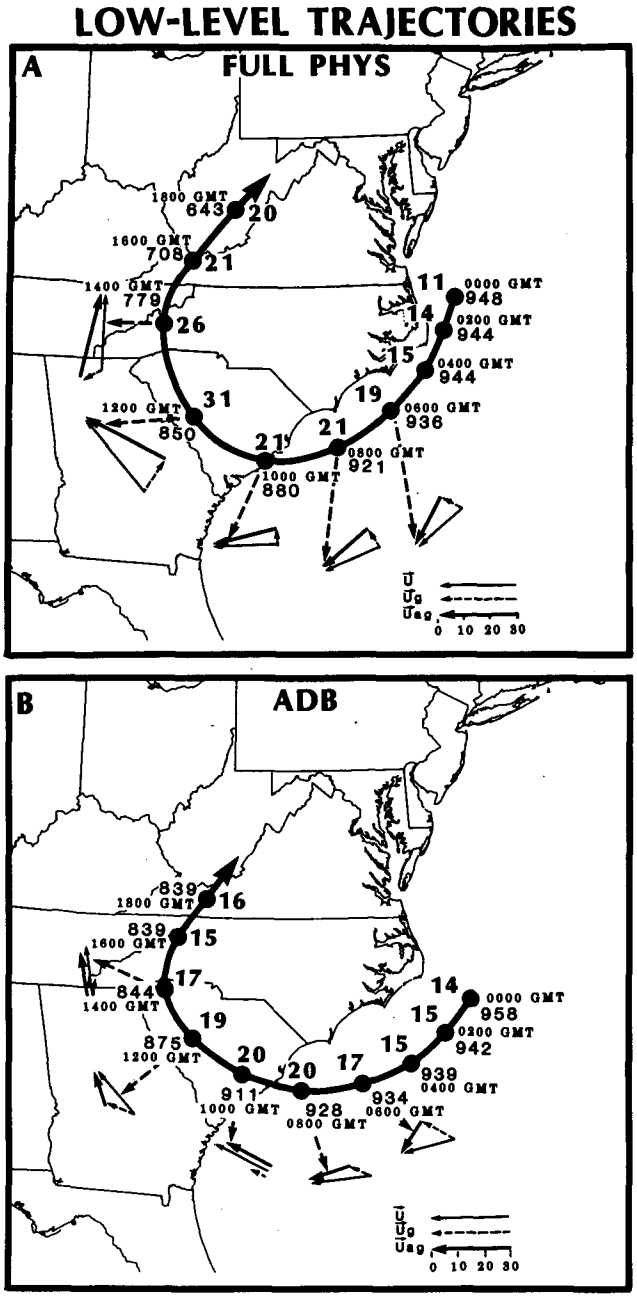

FIG. 19. Low-level trajectory from the (a) full physics simulation (FULL PHYS) and (b) adiabatic simulation (ADB) initialized as described in section 5. Two-hourly positions, total wind speed (m s^{-1}), and pressure (mb) indicated. Vector representation for total wind (U), geostrophic wind (U_g), and ageostrophic wind (U_{ag}) presented at 2 h intervals from 0600 through 1400 UTC. Vectors defined and lengths scaled (m s^{-1}) in bottom right corner.

and U_g remains large (see Table 5). Given that this imbalance is sustained over a significant portion of the trajectory due to the change in the pressure gradient force, the parcel begins to accelerate at 10Z/18 (Table 5) and turns to the right toward the general direction of the low-level geostrophic wind vector. As the parcel ascent increases from -5.7 to -8.7 $\mu b\ s^{-1}$ between 09Z/18 and 10Z/18 (derived from the trajectory computations), it rapidly approaches 850 mb by 12Z/18 during the parcel's interaction with the coastal front (Fig. 15c). The vertical shear of the geostrophic wind in this area is such that an angle exceeding 80° is maintained between U and U_g through 12Z/18, and consequently the magnitude of U_{ag} continues to increase and exceeds 30 m s^{-1}. Thus, the parcel turns to the right and rapidly accelerates toward the northwest. It is not until after 13Z/18 that U becomes directed to the right of the U_g and the parcel begins to decelerate as it continues to rise through the 700 mb level (an ascent that is related, in part, to latent heat release as indicated by the increasing θ and decreasing q in Table 5).

The trajectory from FULL PHYS confirms that the initial acceleration of the parcel and its change in direction from a northeast, to a more east, then a southeast direction is related to the initial modest change in the pressure gradient force experienced by the parcel (as indicated by the change in direction of U_g listed in Table 5). This change is principally due to the westward movement of the parcel toward the developing coastal trough where the pressure gradient force is changing with time. However, the large imbalance represented by the sudden increase in the magnitude of U_{ag} to values approaching 40 m s^{-1} at 11Z/18 (Fig. 18c2) *is principally due to the vertical displacement of the parcel through the baroclinic region associated with the coastal front.*

These trajectory results agree with Durst and Sutcliffe's (1938) and Godson's (1950) hypothesis on the association between organized vertical motion patterns and horizontal acceleration. The results also confirm Newton and Palmén's (1963) discussion of the relationship between vertical motion and parcel acceleration in which they state:

> In the simplest case, supposing that there is geostrophic balance at the level of origin of an air parcel, its ascent or descent in a baroclinic field will carry it to levels where the horizontal pressure gradient is stronger or weaker, and lateral motion across the isobars results from the imbalance created between the Coriolis and pressure gradient forces. (p. 115).

In effect, the rapid development of the LLJ within 3 h represents a three-dimensional adjustment process in which parcels respond to changing pressure gradient forces due not only to horizontal displacement, but also to their vertical displacement within a baroclinic environment.

6. Effects of the LLJ on surface cyclogenesis and upper-level features near the STJ

The results from the previous section show that dynamic and diabatic processes *combine* to produce the development of an inverted trough along the coast that

TABLE 5. Listing for lower-level trajectories from adiabatic simulation (ADB) and full physics simulation (FULL PHYS) (Fig. 19) as described in section 5. Total wind (U), geostrophic wind (U_g), ageostrophic wind (U_{ag}), and pressure (p) listed as for Table 3. Potential temperature (θ) is in K and mixing ratio (q) is in g kg^{-1}.

	Low-level trajectory from ADB						Low-level trajectory from FULL PHYS					
Hour	U	U_g	U_{ag}	θ	p	q	U	U_g	U_{ag}	θ	p	q
04Z/18	63 15	100 7	38 10	277	939	2.3	36 15	83 13	336 12	275	944	3.2
06Z/18	79 17	118 11	39 11	277	934	2.3	50 19	124 6	30 18	278	936	4.0
08Z/18	95 20	113 7	86 13	277	928	2.2	71 21	149 7	51 21	282	921	4.7
09Z/18	105 19	115 6	100 13	277	921	2.1	78 21	183 4	67 22	283	907	4.9
10Z/18	117 20	118 3	116 17	277	911	2.0	94 21	249 8	87 28	284	880	4.6
11Z/18	129 20	132 7	127 13	277	894	1.5	120 27	246 19	97 41	285	857	4.3
12Z/18	138 19	113 7	150 13	277	875	1.7	138 31	218 12	116 32	285	850	4.2
14Z/18	170 17	182 2	169 15	278	844	2.0	181 26	62 6	192 30	289	779	3.5
16Z/18	205 15	219 10	182 6	281	839	2.3	215 21	212 14	216 8	291	708	2.6
18Z/18	228 16	226 5	229 22	281	839	2.3	218 20	220 19	142 1	293	643	1.7

represents the initial phase of secondary cyclogenesis as the primary surface trough remains west of the Appalachian Mountains. Between 12Z/18 and 00Z/19, the lowest pressure in the inverted trough decreases at about 1 mb h^{-1}. During this initial development phase, the cyclonic circulation appears to be confined to the lower troposphere. As shown by Uccellini et al. (1984, 1985) and Bosart and Lin (1984), a second phase of explosive development commences as a polar jet/trough system approaches the coast around 06Z/19, when the surface cyclone deepens at a rate of 3 mb h^{-1} and the cyclonic circulation extends through a deeper portion of the troposphere.

In FULL PHYS, the concentration of the initial pressure falls along the coast occurs simultaneously with the rapid development of the LLJ. This linkage is consistent with Kocin and Uccellini's (1985a,b) survey of 18 cases of major East Coast snowstorms, for which 1) the LLJ is generally directed from east-southeast toward the west-northwest at a significant angle to the coastline and 2) the sea-level pressure appears to decrease as the LLJ develops on the anticyclonic side of an upper-level jet (usually in the exit region of a polar jet).

In this section, the association between the LLJ and the early phase of secondary cyclogenesis is described. A feedback mechanism is also discussed in which the LLJ is related to the enhancement of the cross-contour upper-level ageostrophic flow and associated divergence along the axis of the STJ which contributes further to cyclogenesis and heavy precipitation.

a. The relationship of the LLJ to the surface pressure falls along the coast

In an analysis of mass divergence profiles for 12Z/18, Uccellini et al. (1984) show that the only mass divergence in the region of maximum surface pressure falls apparently occurred between 700 and 900 mb (see Fig. 15; profile D in Uccellini et al., 1984), coincident with the entrance region of the LLJ extending northwestward from 900 to 700 mb (Fig. 2d). In FULL PHYS, the development of the surface trough along the coast at 12Z/18 (Fig. 15b) occurs in the entrance region of the LLJ (Figs. 16d and 18) between the ascending branch of the indirect circulation located over the Appalachian Mountains and the descending branch located 300 to 400 km off the coast (Fig. 17b).

To determine the effect of the LLJ in the initial decrease of sea-level pressure, the mass flux divergence is computed through 21Z/18 for the areas indicated in the map inset in Fig. 21. The areas coincide with both the region of maximum SLP falls (as measured by 3 h tendencies) and the entrance region of the LLJ as simulated in FULL PHYS. The mass flux divergence, which is averaged for 44 grid elements within the areas, is related to the surface pressure tendency by

$$\frac{\partial p_S}{\partial t} = +\int_{\sigma=1}^{\sigma=0} \nabla_\sigma \cdot \left(\frac{\partial p}{\partial \sigma}\mathbf{U}\right) d\sigma, \qquad (1)$$

in which $\partial p/\partial\sigma$ is a measure of mass between sigma surfaces.

At 06Z/18, the mass divergence profile for FULL PHYS indicates relatively weak mass divergence in three layers over the Southeast Coast, one centered near 650 mb, another near 400 mb, and one near 200 mb (Fig. 20a1). This profile is representative of the mass divergence structure at the end of the first 6 h in which the model simulated a SLP decrease of only 2 mb. While a deeper layer of mass divergence develops between 700 and 300 mb by 12Z/18, the mass divergence in the layer below 800 mb increases by an order of magnitude to near 20×10^{-3} mb s^{-1} (Fig. 20a1). This increase in the low-level mass divergence coincides with the rapid development of southeasterly winds in the western portion of the volume without a similar increase in the eastern portion (i.e., the entrance region of the LLJ) and contributes, in part, to a 4 to 5 mb decrease in the SLP along the Carolina coast between 06Z/18 and 12Z/18 (see Figs. 15a and 15b). Also evident from 09Z/18 through 15Z/18 is a shallow layer

TOTAL MASS DIVERGENCE

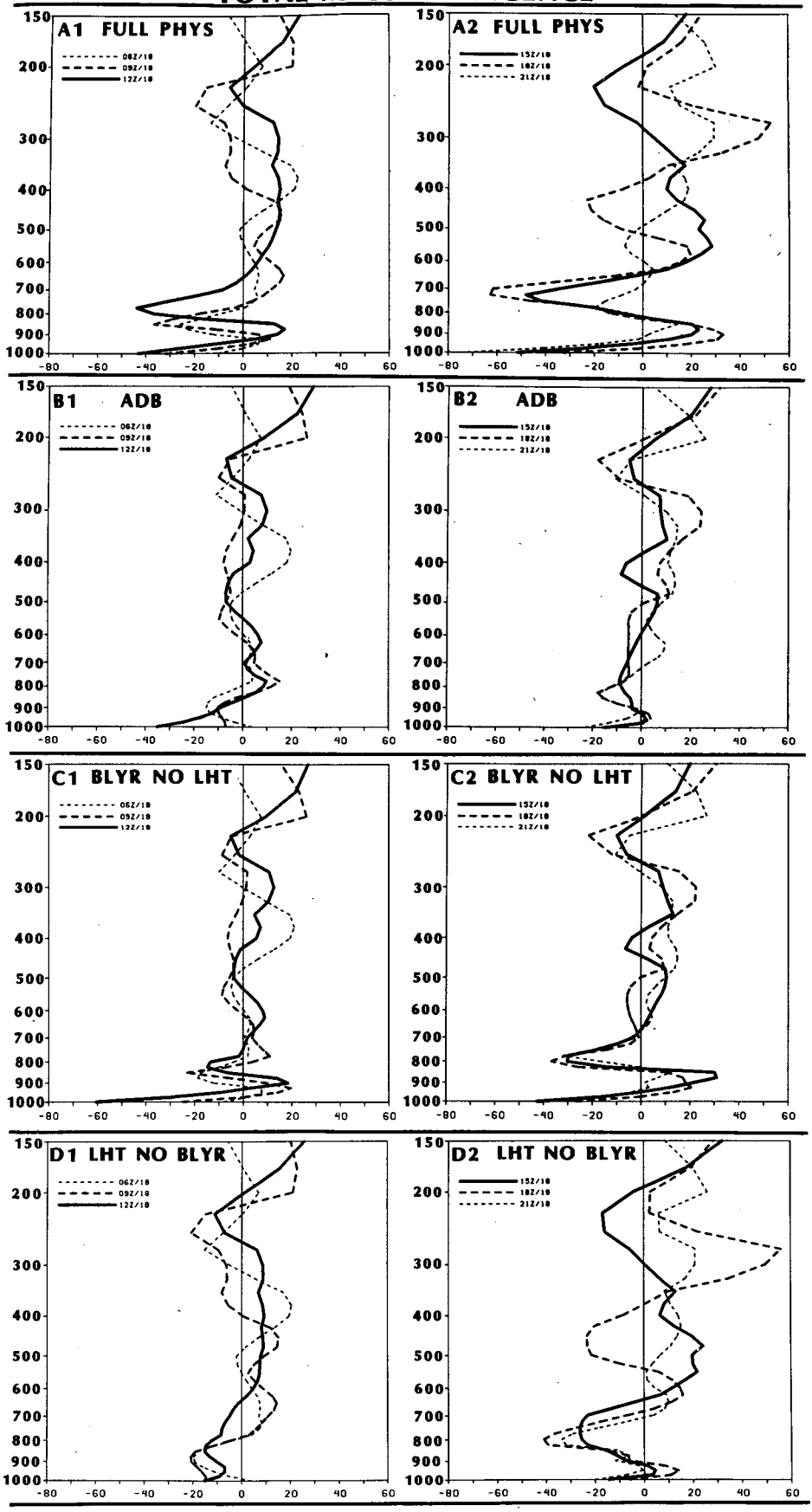

of mass convergence below the 900 mb level, which is consistent with the increasing absolute vorticity associated with the developing inverted trough along the coast. By 18Z/18, the relative maximum in the mass divergence still persists within the entrance region of the LLJ, increasing to 32×10^{-3} mb s^{-1} (Fig. 20b). Simultaneously, the upper-level divergence also increases in magnitude. These persistent regions of mass divergence in the upper and lower troposphere are accompanied by decreasing SLP that marks the initial phase of secondary cyclogenesis along the coast.

Between 18Z/18 and 21Z/18, the low-level mass divergence begins to diminish and a more organized upper-level divergence pattern becomes the dominant factor, as the STJ and its associated divergence pattern shift southward. As the trough originally over the central United States begins to approach the region after 00Z/19, the upper-level divergence pattern becomes an increasingly important factor for the coastal cyclogenesis by 06Z/19 and dominates at 12Z/19 (Petersen et al., 1985). During this period, the lower troposphere is marked by increasing mass convergence as the cyclone appears to intensify over a deeper portion of the lower troposphere. These results confirm earlier findings (Uccellini et al., 1984, 1985; Bosart and Lin, 1984) which show that the *rapid development phase* of the Presidents' Day cyclone occurred as the polar jet/trough system overtook the already developing coastal system.

The mass divergence profiles computed for ADB (Figs. 20b1 and 20b2), BLYR NO LHT (Figs. 20c1 and 20c2), and LHT NO BLYR (Figs. 20d1 and 20d2) illustrate the contribution of the various physical processes to the initial development of this storm. The mass divergence profiles for ADB display only a weak maximum near 800 mb at 09Z/18 and 12Z/18 and a more organized upper-level maximum after 18Z/18. The low-level maximum develops as southeasterly winds in the lower branch of the indirect circulation increase with time (Figs. 8b, 9a, and 9b). However, since the magnitudes of the maximum wind speed and associated horizontal gradients are weaker for the LLJ in ADB (note that the wind speed increase along the low-level trajectory in Fig. 19b is only 2 m s^{-1} between 06Z/18 and 12Z/18), the lower-tropospheric mass divergence remains smaller when compared to FULL PHYS. The magnitude of the upper-level divergence also remains smaller in ADB throughout the entire 24 h simulation.

In BLYR NO LHT, the mass divergence profiles (Figs. 20c1 and 20c2) are dominated by a pronounced maximum in the mass divergence near the 850 mb level that develops between 06Z/18, 09Z/18, and 12Z/18, during which time the SLP begins to decrease and an inverted trough develops (Fig. 11). The striking feature in this simulation is that above 700 mb, the mass divergence profiles for BLYR NO LHT are very similar to the ADB profiles, indicating that the initial development of the inverted trough prior to 15Z/18 in BLYR NO LHT is primarily related to the low-level divergence maximum. However, the lack of deepening of the inverted trough *after* 15Z/18 is probably related to the minimal development of the upper-level divergence (Fig. 20c2) compared to that in FULL PHYS (Fig. 20a2).

For the LHT NO BLYR simulation, the mass divergence profiles illustrate that the impact of including the latent heat release is generally maximized above 700 mb, where the divergence profiles (Figs. 20d1 and 20d2) are nearly identical to those from FULL PHYS. However, below 700 mb, the LHT NO BLYR profiles are similar to those from ADB with no indication of a low-level maximum in the mass divergence being sustained when latent heat is the only physical process included in the model simulation. Given that the major difference between the FULL PHYS and LHT NO BLYR divergence profiles is confined to the lower troposphere, it appears that the lack of mass divergence near 850 mb could account for the lack of development of an inverted trough along the Southeast Coast in the LHT NO BLYR simulation (Fig. 13).

These results demonstrate that 1) the PBL physics and latent heat release have a significant effect on the lower- and upper-level mass divergence maxima, respectively, 2) the initiation of the secondary cyclogenesis along the coast is strongly influenced by the low-level mass divergence in the entrance region of a rapidly developing LLJ that acts to focus SLP falls along the coast, and 3) the continued development of the inverted trough and cyclone along the coast prior to 00Z/19 is sustained by the upper-level mass divergence along the axis of the STJ that is enhanced by the latent heat release.

b. Effect of LLJ development on the upper-level features

As shown by Uccellini et al. (1984), the decreasing distance between the upper-level ridge and trough axes contributes to parcel accelerations and associated increasing upper-level divergence along the axis of the STJ near the ridge crest at 12Z/18. The decreasing

FIG. 20. Vertical profiles of area-averaged mass flux divergence ($10 = 10 \times 10^{-3}$ mb s^{-1}) computed for 0600 (thin dashed), 0900 (thick dashed), and 1200 UTC (solid) in the left column and 1500 (solid), 1800 (thick dashed), and 2100 UTC (thin dashed) in the right column. (a) Profiles from full physics simulation (FULL PHYS); (b) profiles from adiabatic simulation (ADB); (c) profiles from boundary layer simulation with no latent heat (BLYR NO LHT); and (d) profiles from latent heat simulation with no boundary layer (LHT NO BLYR). The profiles are computed for the areas along the Georgia to Middle Atlantic coasts depicted on map inset for times shown in Fig. 21.

wavelength is due to the decrease in the propagation rate of the ridge without a corresponding decrease in the eastward propagation rate of the trough in the central United States. Using a quasi-geostrophic approach, Atlas (1987) shows that the decreasing wavelength during the period of rapid cyclogenesis on 19 February increases the vorticity gradient between the trough and ridge axes and thereby contributes to an increase of vorticity advection and associated upper-level divergence over the cyclone during its rapid development phase.

As indicated in the map inset in Fig. 21, the 332 K ψ values are larger near the ridge axis in FULL PHYS as compared to ADB. The increases in ψ are associated with a more pronounced ridge and slower eastward displacement of the 332 K ridge crest in FULL PHYS, which is also reflected by the 3 h ψ tendency field over the Appalachian region where the ψ falls in ADB are twice as large as those in FULL PHYS (not shown). For the area depicted in the map inset (Fig. 21), the difference between the adiabatic and full physics simulations is reflected by the profiles of the geopotential height (ϕ) tendency derived on pressure surfaces between 09Z/18 and 12Z/18 (Fig. 21a). The vertical profiles of the ϕ tendency are significantly less negative above 700 mb for FULL PHYS due principally to the large differences in the local temperature tendencies for the same region (Fig. 21b). In ADB, 15 to 20 K day^{-1} cooling rates are diagnosed between 950 and 500 mb, while FULL PHYS cooling rates generally range between 0 and 10 K day^{-1} below 500 mb, resulting in smaller negative ϕ tendencies and thus a slower eastward displacement of the ridge.

The relative importance of the various physical processes that could act to reduce the cooling rates and enhance the magnitude of the upper-tropospheric ridge is assessed through an evaluation of the thermodynamic equation,

$$\frac{\partial T}{\partial t} = \mathbf{U} \cdot \nabla_p T + \frac{Q}{c_p} - \omega\left(\frac{\partial T}{\partial p} - \frac{RT}{c_p P}\right), \qquad (2)$$

(where Q is the heating rate due to latent heat release, c_p is specific heat under constant pressure, and R is the universal gas constant). All the terms on the right-hand side of (2) are averaged over the 3 h between 09Z/18 and 12Z/18 for the area shaded in the map inset in Fig. 21 for ADB and FULL PHYS.

A significant difference exists between these two simulations for all three terms in Eq. (2). Warm air advection is larger in FULL PHYS throughout the entire troposphere below 450 mb, with the maximum advection located near 850 mb (Fig. 21c). The increased warm air advection associated with the general increase in the magnitude of the low-level winds in FULL PHYS accounts for a significant portion of the difference in the local temperature tendency beneath the 800 mb level. Heating rates of 10 to 25 K day^{-1} associated with latent heat release between 800 and 450 mb (Fig. 21d) are slightly larger than the maximum warming associated with the warm air advection below 700 mb and contribute significantly to the difference in the local temperature tendency between ADB and FULL PHYS, especially above 750 mb. The last term in Eq. (2), which combines the effects of vertical temperature advection and adiabatic expansion and acts to offset the warming effects of the other two terms, is negative throughout for both simulations. The increased horizontal temperature advection associated with the development of the LLJ combined with latent heat release is sufficient to offset the greater cooling associated with the enhanced ascent pattern in FULL PHYS to produce a relatively warmer domain and better-defined upper-level ridge compared to ADB.

7. Summary

A series of numerical simulations of the Presidents' Day cyclone isolates the active roles of upper-tropospheric jet streaks, the oceanic PBL, and latent heat release in the secondary cyclogenesis observed along the East Coast of the United States on 18–19 February 1979. Model simulations with and without diabatic processes associated with heat and moisture fluxes in the oceanic PBL and grid-resolvable and convective precipitation show that these processes, in conjunction with the jet streak circulation patterns, are necessary for the initial development of the storm system along the coast. However, neither the jet alone nor the combinations of either the jet-induced circulation with latent heat release or the jet-induced circulation with PBL processes is sufficient to yield a satisfactory simulation of the LLJ and the initial phase of secondary cyclogenesis. *Therefore, a synergistic interaction must exist among these processes to account for the secondary cyclogenesis and associated rapid changes in the mass, momentum, and moisture fields for this case.*

The numerical simulations indicate the following sequence of events marked the initial development phase of the Presidents' Day cyclone:

1) Increasing divergence along the axis of an upper-tropospheric STJ is associated with the development of an indirect circulation displaced to the anticyclonic side of the STJ and extending through the entire depth of the troposphere. The lower branch of the indirect circulation amplifies over the southeastern United States with a significant ageostrophic wind component directed from the oceanic PBL across the coastline toward the Appalachian Mountains.

2) Sensible heating and moisture flux within the oceanic PBL reduce the static stability east of the Carolina coast. Furthermore, the heat and moisture fluxes warm and moisten the lower branch of the indirect circulation, enhancing precipitation rates and latent heat release west of the coastline.

3) The sloped orientation of the lower-tropospheric

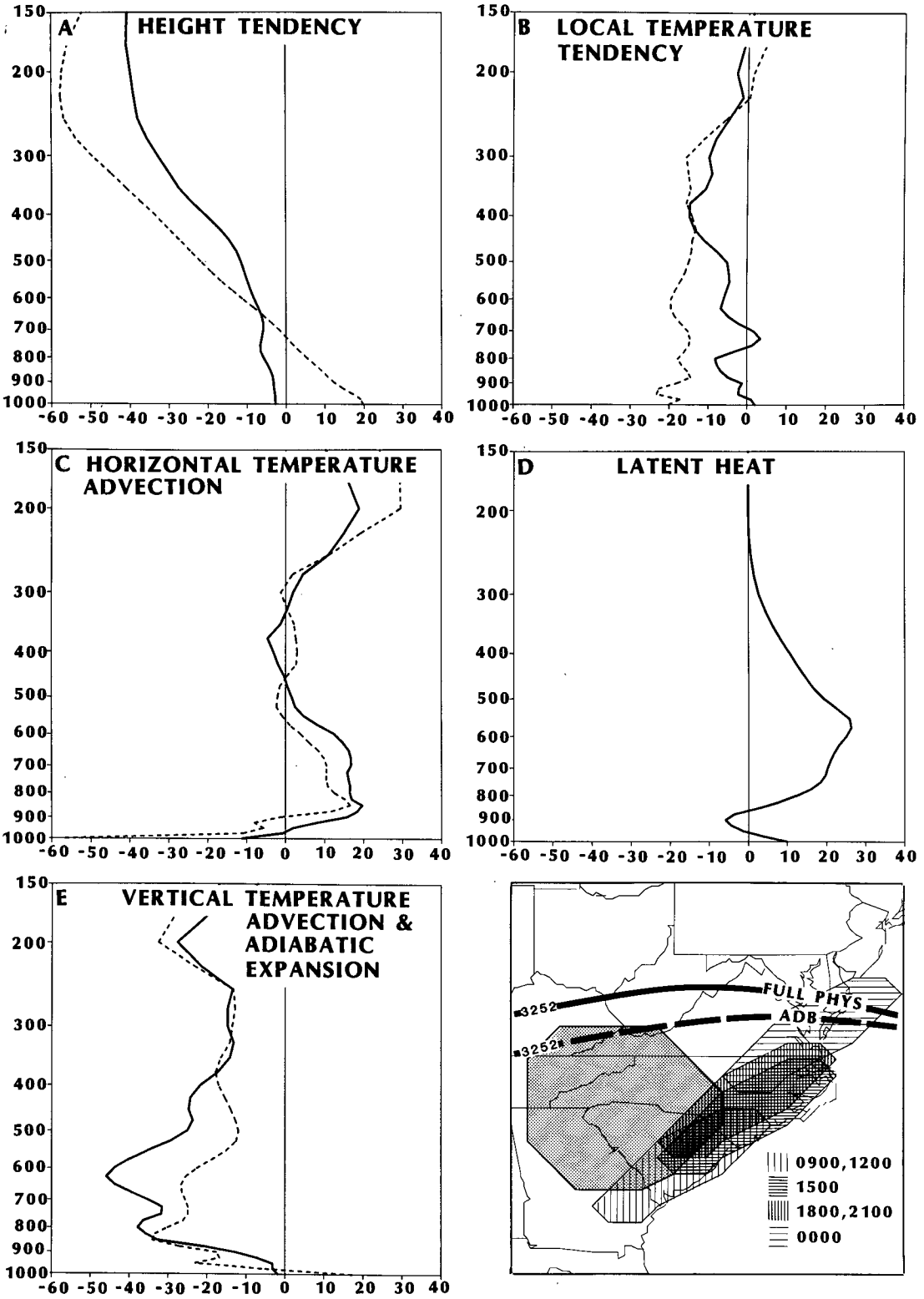

FIG. 21. Vertical profiles of areal- and time-averaged tendencies for a 3 h period between 0900 and 1200 UTC 18 February for the lightly shaded inland region in the map inset. (a) Geopotential height (20 = 20 m height change over 3 h), (b) local temperature (K day^{-1}) changes, (c) temperature changes (K day^{-1}) due to horizontal temperature advection, (d) temperature changes (K day^{-1}) due to latent heat release, and (e) vertical temperature advection and expansion. Solid lines are for the full physics simulation (FULL PHYS) and dashed lines are for the adiabatic simulation (ADB), where applicable. The position of a representative ψ_m contour (3.252×10^5 m^2 s^{-2}) is also shown in map inset for ADB (dashed) and FULL PHYS at 1200 UTC 18 February (solid).

isentropic surfaces west of the coastline, the merging of the lower branch of the indirect circulation associated with the STJ and the upper branch of a direct circulation associated with the coastal front and latent heat release all contribute to a significant vertical displacement of parcels crossing the coastline within the lower branch of the indirect circulation.

4) The vertical displacement of the parcels in a baroclinic environment (in which both the magnitude and direction of the pressure gradient force change significantly with height) is associated with a rapid increase in the magnitude of the ageostrophic wind component along the coast within a 2 to 3 h period. This imbalance subsequently leads to parcel acceleration and to the rapid formation of a LLJ that slopes upward from the oceanic PBL toward the 700 mb level over the Appalachian Mountains. The sudden onset of the LLJ is a manifestation of three-dimensional adjustment processes as the transverse circulation associated with the upper-level jet is significantly modulated by diabatic processes and coastal frontogenesis in a strongly baroclinic regime.

5) The accelerations associated with the developing LLJ are responsible for a sudden increase in the lower-tropospheric mass flux divergence in the entrance region of the LLJ. The mass divergence maximum in the entrance region of the LLJ is an important factor in focusing the decrease in SLP along the Southeast Coast that constitutes the initial development phase of the secondary cyclone as the primary surface system weakens and fills over the Ohio Valley.

6) The development of the LLJ enhances the warm air advection and moisture flux to the north and west of the developing surface low. The increased warm air advection and latent heat release (associated with resolvable grid-scale precipitation) act to increase the magnitude of the upper-level ridge. Furthermore, the propagation rate of the upper-level ridge is decreased while the upper-level trough over the central United States continues to propagate eastward, effectively reducing the wavelength between the trough and ridge axes.

The processes involved in the development of the LLJ, coastal cyclogenesis, and the enhancement of the upper-level ridge interact in a mutually supportive way. The sensible and latent heating in the ocean-influenced PBL and coastal frontogenesis contribute to the vertical displacement of parcels entering the LLJ, resulting in significant ageostrophy and subsequent horizontal accelerations. These accelerations contribute to the decrease of the SLP along the coast and to the increase in 1) the magnitude of the warm air advection, 2) moisture transport over a broad region in the southeastern United States, and 3) the precipitation and associated latent heat release. The warm air advection and latent heat release act to enhance the magnitude of the upper-level ridge and slow its eastward movement as the trough approaches the East Coast from the central United States. Parcels moving along the axis of the STJ approach the ridge axis, cross toward lower ψ_m values, and accelerate. The acceleration, associated with the decreasing distance between the trough and ridge axes, is accompanied by increasing upper-level divergence. The upper-level divergence enhances the ascending branch of the indirect circulation in which the LLJ is embedded. The process thereby supports further development of the LLJ and surface cyclone.

This sequence represents a positive feedback mechanism which sustains the early development of the Presidents' Day cyclone in a manner similar to the "self-development" concept identified by Sutcliffe and Forsdyke (1950) and discussed by Palmén and Newton (1969, pp. 324–326). If the low-level warming related to temperature advections or diabatic processes is not sufficiently strong, the upper-level divergence between the trough and the ridge axes will not increase, thus disrupting the feedback effect that perpetuates the development of the LLJ and associated temperature advection and low-level mass divergence patterns that are focused along the Southeast Coast. This disruption occurs after 15Z/18 in ADB, BLYR NO LHT, and LHT NO BLYR. These three simulations lack the sustained warming associated with temperature advection and diabatic processes that contribute to the mass divergence maxima in the lower and upper troposphere needed to support the continued development of the surface trough for this case.

This model experiment indicates that, since the dynamic and diabatic processes act in a synergistic manner, it is not possible to designate one process as more important than another for the formation of this coastal storm. Furthermore, it is difficult to separate the relative importance of upper- and lower-tropospheric forcing mechanisms since processes near the top and bottom of the troposphere interact to influence the evolution of the jet streak system, surface cyclone, and associated vertical circulation patterns diagnosed throughout the entire extent of the troposphere.

Several issues are raised by this study that merit further research. One issue concerns the role of coastal frontogenesis in the development of the LLJ and the subsequent decrease in the SLP along the coast. This model study is in agreement with Bosart et al.'s (1972) and Ballentine's (1980) emphasis on the importance of surface heat fluxes from the ocean in the development of the coastal front. Nevertheless, more research is needed to determine how this physical process appears to combine with a jet streak–related circulation that spans the entire troposphere to yield a deformation field that focuses maximum frontogenesis along the coast. It appears from the FULL PHYS simulation that mesoscale model output can provide a synthetic synoptic database to study this problem.

Another issue concerns the applicability of these re-

sults that point to the existence of an indirect circulation in the initial development phase to other cases of East Coast cyclogenesis. Although the initial development of many of the coastal cyclones documented by Kocin and Uccellini (1985a,b) also occur on the anticyclonic side of an upper-level jet and within an indirect circulation, the indirect circulation is typically located in the exit region of the polar jet streak associated with a well-defined trough propagating toward the coast. Kaplan et al. (1982b) and Kocin et al. (1985c) present evidence from numerical simulations of the 6 April 1982 and 8 March 1984 East Coast snowstorms, respectively, that secondary coastal cyclogenesis commences as the exit region of the polar jet approaches the coast. The initial development of the QE II storm also occurred on the anticyclonic side-exit region of an upper-level jet (Gyakum, 1983a), which likely played a role in the rapid cyclogenesis, as noted by Uccellini (1986). Although these cases have characteristics unique to each storm, a common feature is the possible enhancement of the indirect transverse circulation by diabatic processes, especially in the oceanic PBL. While the synergistic interaction between jet-related circulation patterns and diabatic processes may be applicable to other cases, additional diagnostic-model studies are needed for each case to fully test this hypothesis.

Finally, the issue concerning whether the results presented here are more representative of the real atmosphere or a numerical model system with all of its limitations (grid resolution, parameterization of subgrid-scale physical processes, initial data) still remains and needs to be further explored. For example, FULL PHYS produced a PBL depth of 120 mb east of the Virginia and Carolina coastline, which compares to 200 mb estimated for this case by Bosart (1981). These differences may have significant impact on the evolution of the LLJ and developing cyclone and point to deficiencies in the model and/or the database. Future model-based studies could benefit from an expanded database to better document the complex interactions between the dynamic and thermodynamic processes that combined to produce the Presidents' Day snowstorm. Data that cover a large domain on either side of the coastline with mesoscale resolution would be helpful not only in diagnosing the processes and in initializing and verifying numerical forecasts, but also in developing better physical parameterization schemes needed for more accurate numerical simulations. It is anticipated that datasets and model simulations that resolve the mesoscale structure along the coastline and near the Gulf Stream would be particularly important for improving diagnostic/model-based studies and would lead to an increased understanding of cyclogenesis along the East Coast of the United States.

Acknowledgments. The authors thank Miss Kelly Wilson for typing the numerous drafts of this manuscript. Discussions with Drs. Michael Kaplan, John Zack, and Lance Bosart have been helpful during the course of this study. Dr. Daniel Keyser's review was also helpful in clarifying portions of this manuscript. Thanks to Mr. Robert Aune (STX Systems Corporation) and Mr. Jeffrey S. Whitaker (Florida State University) for their help in developing model and post-processing software used in this study. We are grateful for the thorough reviews provided by Drs. Chester Newton and Norman Phillips, which made important contributions to the final version of this paper.

APPENDIX

A Summary of the PBL Formulation for Momentum, Heat, and Moisture Fluxes and for Surface Moisture

The fluxes of momentum, heat, and moisture into the model PBL are parameterized in terms of transfer coefficients C_H and C_U for heat and momentum, nondimensional coefficients k and P_{r0},[7] the von Kármán constant and turbulent Prandtl number, respectively, the roughness length z_0, the boundary layer depth h, the surface values θ_0 and q_0 of virtual potential tempepature and specific humidity, respectively, the mean boundary layer values $\mathbf{V}_m$, θ_m, and q_m of wind, virtual potential temperature, and specific humidity, respectively, and density ρ. The surface stresses (i.e., momentum fluxes) are

$$\tau_x = \rho C_U^2 |\mathbf{V}_m|^2 \cos(\phi + \theta) \tag{A1}$$

$$\tau_x = \rho C_U^2 |\mathbf{V}_m|^2 \sin(\phi + \theta), \tag{A2}$$

where ϕ is the angle between $\mathbf{V}_m$ and the x-coordinate and θ is given by

$$\theta = \arcsin\left[\frac{C_U}{K} \mathrm{B}\ \mathrm{sgn}(f)\right], \tag{A3}$$

where f is the Coriolis parameter and B is one of Yamada's (1976) universal functions. The fluxes of heat and moisture are, respectively,

$$H = -\rho c_p C_U C_H |\mathbf{V}_m|(\theta_m - \theta_0) \tag{A4}$$

$$Q = -\rho C_H C_U |\mathbf{V}_m|(q_m - q_0). \tag{A5}$$

More information on Eqs. (A1)–(A5) can be found in Kaplan et al. (1982a).

The value of z_0 over land is determined as a function of terrain elevation z_s according to

$$z_0 = (0.2 + 2.0 \times 10^{-4} z_s). \tag{A6}$$

Over water, z_0 is a function of the mean boundary layer wind according to

$$z_0 = 1.3 \times 10^{-6} |\mathbf{V}_m|^2. \tag{A7}$$

[7] In the model, $k = 0.35$ and $P_{r0} = 0.74$, except $k = 0.4$ in evaluation of θ using (A3).

The values of C_U and C_H are computed differently for various stability conditions determined on the basis of the bulk Richardson number

$$\mathrm{Ri}_b = gh(\theta_m - \theta_0)/(\theta_m |V_m|^2). \quad \text{(A8)}$$

If Ri_b is greater than zero, the boundary layer is considered to be stable. The unstable case ($\mathrm{Ri}_b < 0$) can be subdivided into two cases on the basis of $\xi(\mathrm{Ri}_b)$ computed according to the approximate expression

$$\xi \sim \mathrm{Ri}_b\left[5.4 + \ln\left(\frac{h}{z_0}\right)\right]. \quad \text{(A9)}$$

If $\xi > -10.0$, the near-neutral case is considered. If $\xi < -10.0$, the free convection case is considered.

The treatment of the stable case is described in Kaplan et al. (1982a). It involves an iterative solution for Yamada's (1976) universal functions A, B, and C. Once these functions are found, C_U and C_H can be computed from

$$C_U = \frac{k}{\{[\ln(h/z_0) - \mathrm{A}]^2 + \mathrm{B}^2\}^{1/2}} \quad \text{(A10)}$$

$$C_H = \frac{k}{P_{r0}[\ln(h/z_0) - C]}. \quad \text{(A11)}$$

There is an error in Kaplan et al.'s (1982a) Eq. (35); that equation should be

$$f'(\xi_I) = f(\xi_I)\left(\frac{1}{\xi} - \frac{c}{\ln(h/z_0) - c} - \frac{2[\mathrm{AA}' - \ln(h/z_0)\mathrm{A}' + \mathrm{BB}']}{[\ln(h/z_0) - \mathrm{A}]^2 + \mathrm{B}^2}\right),$$

where the symbols are defined in the referenced article.

The near-neutral case requires the universal functions A, B, and C, which are computed using the first three equations in Table 2 of Kaplan et al. (1982a) with ξ given by (A9). Equations (A10) and (A11) are used to compute C_U and C_H.

The unstable free convection case is separated into two schemes, over land and over water. Over land, C_U^2 and $C_U C_H$ are obtained from a cubic polynomial fit to Businger (1973). Over water, C_U^2 and $C_U C_H$ are calculated from a linear curve fit to Stage and Businger (1981). In either case, the value for B needed in Eq. (A3) is obtained as for the near-neutral case discussed above. When the boundary layer is unstable, the convectively driven wind can be stronger than the mean boundary layer wind $|\mathbf{V}_m|$. This convective wind speed U_{CONV} is computed according to

$$U_{\mathrm{CONV}} = 0.7\left[0.7 C_U C_H (\theta_0 - \theta_m)\frac{gh}{\theta_m}\right]^{1/2}, \quad \text{(A12)}$$

following Deardorff (1972) and is used in place of $|\mathbf{V}_m|$ in Eqs. (A1), (A2), (A4), and (A5) whenever $U_{\mathrm{CONV}} > |\mathbf{V}_m|$.

To compute the moisture flux in Eq. (A5), surface moisture must be specified. Surface moisture is parameterized in terms of surface temperature T_s and the mean boundary layer specific humidity q_m. The surface specific humidity q_0 is computed in the following sequence of steps:

1) Compute

$$q_s' = \frac{\epsilon e_s(T_s)}{P_s - e_s(T_s)},$$

where $e_s(T_s)$ is the saturation vapor pressure at T_s, P_s is the surface pressure, and ϵ is the ratio of the molecular weight of water to that of dry air.

2) Set $\alpha = 1$ over water, 0.2 over land where $z_s \leq 700$ m, and 0.1 over land where $z_s > 700$ m. Here z_s is the surface elevation.

3) $q_0 = \alpha q_s' + (1 - \alpha) q_m$.

Note that, over water, q_0 is q_s' and T_s is given by monthly average of sea surface temperature. The value T_s is the temperature over land and is determined from the radiative parameterization described by Kaplan et al. (1982a).

REFERENCES

Anthes, R. A., Y.-H. Kuo and J. R. Gyakum, 1983: Numerical simulations of a case of explosive marine cyclogenesis. *Mon. Wea. Rev.*, **111**, 1174–1188.

Atlas, R., 1987: The role of oceanic fluxes and initial data on the numerical prediction of an intense coastal storm. *Dyn. Atmos. Oceans*, **10**, 359–388.

Ballentine, R. J., 1980: A numerical investigation of New England coastal frontogenesis. *Mon. Wea. Rev.*, **108**, 1479–1497.

Bjerknes, J., 1951: Extratropical cyclones. *Compendium of Meteorology*, T. F. Malone, Ed., Amer. Meteor. Soc., 577–598.

Bosart, L. F., 1981: The Presidents' Day snowstorm of 18–19 February 1979: A subsynoptic-scale event. *Mon. Wea. Rev.*, **109**, 1542–1566.

——, and S. C. Lin, 1984: A diagnostic analysis of the Presidents' Day storm of February 1979. *Mon. Wea. Rev.*, **112**, 2148–2177.

——, C. J. Vanado and J. H. Helsdon, Jr., 1972: Coastal frontogenesis. *J. Appl. Meteor.*, **11**, 1236–1258.

Businger, J. A., 1973: Turbulent transfer in the atmospheric surface layer. *Proc. Workshop on Micrometeorology*, D. A. Haugen, Ed., Boston, Amer. Meteor. Soc., 392 pp.

Cahir, J. J., 1971: Implications of circulations in the vicinity of jet streaks at subsynoptic scales. Ph.D. thesis, Pennsylvania State University, 170 pp.

Chang, C.-B., D. J. Perkey and C. W. Kreitzberg, 1982: A numerical case study of the effects of latent heating on a developing wave cyclone. *J. Atmos. Sci.*, **39**, 1555–1570.

Chou, S.-H., and D. Atlas, 1982: Satellite estimates of ocean-air heat fluxes during cold air outbreaks. *Mon. Wea. Rev.*, **110**, 1434–1450.

Cressman, G., 1959: An operational objective analysis scheme. *Mon. Wea. Rev.*, **87**, 367–374.

Danard, M. B., 1964: On the influence of released latent heat on cyclone development. *J. Appl. Meteor.*, **3**, 27–37.

Deardorff, J. W., 1972: Numerical investigation of neutral and unstable planetary boundary layers. *J. Atmos. Sci.*, **29**, 91–115.

Durst, C. S., and R. C. Sutcliffe, 1938: The importance of vertical motion in the development of tropical revolving storms. *Quart. J. Roy. Meteor. Soc.*, **64**, 75–84.

Gall, R., 1976: The effects of released latent heat in growing baroclinic waves. *J. Atmos. Sci.*, **33**, 1686–1701.

Godson, W. L., 1950: A study of the deviation of wind speeds and

directions from geostrophic values. *Quart. J. Roy. Meteor. Soc.*, **76,** 3–15.

Gyakum, J. R., 1983a: On the evolution of the QE II storm. I: Synoptic aspects. *Mon. Wea. Rev.*, **111,** 1137–1155.

——, 1983b: On the evolution of the QE II storm. II: Dynamic and thermodynamic structure. *Mon. Wea. Rev.*, **111,** 1156–1173.

Haltiner, J. G., and R. T. Williams, 1980: *Numerical Prediction and Dynamic Meteorology.* Wiley and Sons, 477 pp.

Johnson, D. R., and W. K. Downey, 1976: The absolute angular momentum budget of an extratropical cyclone: Quasi-Lagrangian diagnostics. *Mon. Wea. Rev.*, **104,** 3–14.

Kaplan, M. L., J. W. Zack, V. C. Wong and J. J. Tuccillo, 1982a: Initial results from a mesoscale atmospheric simulation system and comparisons with the AVE-SESAME I data set. *Mon. Wea. Rev.*, **110,** 1564–1590.

——, ——, —— and ——, 1982b: A sixth order mesoscale atmospheric simulation system applicable to research and real-time forecasting problems. *Proc. Symp. on Mesoscale Meteorology,* Y. Sasaki, Ed., Norman, OK, CIMMS, 38–84.

——, ——, —— and G. D. Coats, 1984: The interactive role of subsynoptic scale jet streak and planetary boundary layer processes in organizing an isolated convective complex. *Mon. Wea. Rev.*, **112,** 2212–2237.

Keyser, D., and M. J. Pecnick, 1985: Diagnosis of ageostrophic circulations in a two-dimensional primitive equation model of frontogenesis. *J. Atmos. Sci.*, **42,** 1283–1305.

——, and M. A. Shapiro, 1986: A review of the structure and dynamics of upper-level frontal zones. *Mon. Wea. Rev.*, **114,** 452–499.

Keyser, D. A., and D. R. Johnson, 1984: Effects of diabatic heating on the ageostrophic circulation of an upper tropospheric jet streak. *Mon. Wea. Rev.*, **112,** 1710–1724.

Koch, S. E., 1985: Ability of a regional-scale model to predict the genesis of intense mesoscale convective systems. *Mon. Wea. Rev.*, **113,** 1693–1713.

——, W. C. Skillman, P. J. Kocin, P. J. Wetzel, K. F. Brill, D. A. Keyser and M. C. McCumber, 1985: Synoptic scale forecast skill and systematic errors in the MASS 2.0 model. *Mon. Wea. Rev.*, **113,** 1714–1737.

Kocin, P. J., and L. W. Uccellini, 1985a: A survey of major East Coast snowstorms, 1960–1983. Part 1: Summary of surface and upper-level characteristics. *NASA TM 86195,* 101 pp. [NTIS N85-27471.] (Also tentatively accepted for publication as a *Meteorological Monograph.*)

——, and ——, 1985b: A survey of major East Coast snowstorms, 1960–1983. Part 2: Case studies of eighteen storms. *NASA TM 86196,* 214 pp. [NTIS N85-27472.] (Also tentatively accepted for publication as a *Meteorological Monograph.*)

——, ——, J. W. Zack and M. L. Kaplan, 1985c: A mesoscale numerical forecast of an intense convective snowburst along the East Coast. *Bull. Amer. Meteor. Soc.*, **66,** 1412–1424.

——, —— and Ralph A. Petersen, 1986: Rapid evolution of a jet streak circulation in a pre-convective environment. *Meteor. Atmos. Phys.* (formerly *Archiv. Meteor. Geophys. Bioklim.*), **35,** 103–138.

Kuo, H. L., 1974: Further studies of the parameterization of the influence of cumulus convection on large-scale flow. *J. Atmos. Sci.*, **31,** 1232–1240.

Miller, J. E., 1946: Cyclogenesis in the Atlantic coastal region of the United States. *J. Meteor.*, **3,** 31–44.

Molinari, J., 1982: A method for calculating the effects of deep cumulus convection in numerical models. *Mon. Wea. Rev.*, **110,** 1527–1534.

Newton, C. W., and E. Palmén, 1963: Kinematic and thermal properties of a large-amplitude wave in the westerlies. *Tellus,* **15,** 99–119.

O'Brien, J. J., 1970: Alternative solutions to the classical vertical velocity problem. *J. Appl. Meteor.*, **9,** 197–203.

Palmén, E., and C. W. Newton, 1969: *Atmospheric Circulation Systems, Their Structure and Physical Interpretation. Int. Geophys. Ser.,* Vol. 13, Academic Press, 603 pp.

Petersen, R. A., 1975: The role of adiabatic and diabatic processes in the mass budget of extratropical cyclones. Ph.D. thesis, University of Wisconsin, 167 pp.

——, 1986: Detailed three-dimensional isentropic analysis using an objective cross-sectional approach. *Mon. Wea. Rev.* **114,** 719–735.

——, J. J. Tuccillo, K. F. Brill and L. W. Uccellini, 1985: The sensitivity of a mesoscale forecast model to detailed three-dimensional isentropic initial analysis and varied vertical model resolution. *Preprints Seventh Conf. Numerical Weather Prediction,* Montreal, Amer. Meteor. Soc., 83–90.

Sanders, F., and J. R. Gyakum, 1980: Synoptic-dynamic climatology of the "bomb." *Mon. Wea. Rev.*, **108,** 1589–1606.

Stage, S. A., and J. A. Businger, 1981: A model for entrainment into a cloud-topped marine boundary layer. Part I: Model description and application to a cold-air outbreak episode. *J. Atmos. Sci.*, **38,** 2213–2229.

Sutcliffe, R. C., and A. G. Forsdyke, 1950: The theory and use of upper air thickness patterns in forecasting. *Quart. J. Roy. Meteor. Soc.*, **76,** 189–217.

Teweles, S., Jr., and H. B. Wobus, 1954: Verification of prognostic charts. *Bull. Amer. Meteor. Soc.*, **10,** 455–463.

Tuccillo, J. J., 1984: Memory efficient solution to the primitive equations for numerical weather prediction on the CYBER 205. *CYBER 200 Applications Seminar, NASA Conference Publication 2295,* 35–60. [NTIS N84-20208.]

Uccellini, L. W., 1986: The possible influence of upstream upper-level baroclinic processes on the development of the QE II storm. *Mon. Wea. Rev.*, **114,** 1019–1027.

——, and D. R. Johnson, 1979: The coupling of upper- and lower-tropospheric jet streaks and implications for the development of severe convective storms. *Mon. Wea. Rev.*, **107,** 682–703.

——, R. A. Petersen, P. J. Kocin, M. L. Kaplan, J. W. Zack and V. C. Wong, 1983: Mesoscale numerical simulations of the Presidents' Day cyclone: Impact of sensible and latent heating on the pre-cyclogenetic environment. *Preprints Sixth Conf. on Numerical Weather Prediction,* Omaha, Amer. Meteor. Soc., 45–52.

——, P. J. Kocin, R. A. Petersen, C. H. Wash and K. F. Brill, 1984: The Presidents' Day cyclone of 18–19 February 1979: Synoptic overview and analysis of the subtropical jet streak influencing the pre-cyclogenetic period. *Mon. Wea. Rev.*, **112,** 31–55.

——, D. Keyser, K. F. Brill and C. H. Wash, 1985: The Presidents' Day cyclone of 18–19 February 1979: Influence of upstream trough amplification and associated tropopause folding on rapid cyclogenesis. *Mon. Wea. Rev.*, **113,** 962–988.

Yamada, T., 1976: On the similarity functions A, B and C of the planetary boundary layer. *J. Atmos. Sci.*, **33,** 781–793.

Zack, J. W., V. C. Wong, M. L. Kaplan and G. D. Coats, 1984: A model-based investigation of the role of boundary layer fluxes and deep convective processes in the precipitation distribution of East Coast cyclones. *Preprints Tenth Conf. on Weather Forecasting and Analysis,* Clearwater Beach, FL, Amer. Meteor. Soc., 588–595.

——, M. L. Kaplan, and V. C. Wong, 1987: Numerical simulations of the subsynoptic features associated with the AVE-SESAME case. Part 1: The pre-convective environment. *Mon. Wea. Rev.* (in press).